

FINAL REPORT

Augmenting MFL Tools with Sensors That Assess Coating Condition

By

J. Bruce Nestleroth
Energy Systems
Battelle Memorial Institute
505 King Avenue
Columbus, OH 43201

Jason K. Van Velsor
FBS, Inc.
143 Hawbaker Industrial Dr.
Suite 102
State College, PA 16803

Prepared for

U.S. Department of Transportation
Pipeline and Hazardous Materials
Safety Administration
1200 New Jersey Ave., SE
Washington DC 20590
Contract No. DTPH56-06-T-000019
Battelle Project No. G005686

Pipeline Research Council International
1401 Wilson Boulevard
Suite 1101
Arlington, Virginia 22009
Contract No. PR-003-073505
Battelle Project No. N006981

March 16, 2009



This report is a work prepared for the United States Government by Battelle. In no event shall either the United States Government or Battelle have any responsibility or liability for any consequences of any use, misuse, inability to use, or reliance upon the information contained herein, nor does either warrant or otherwise represent in any way the accuracy, adequacy, efficacy, or applicability of the contents hereof.

Public Abstract

External coatings are routinely used to protect transmission pipelines from corrosion; however, coatings may degrade or debond over time enabling corrosion to occur. Transmission pipeline operators often use magnetic flux leakage (MFL) in-line inspection tools to detect metal loss corrosion defects. Rather than finding the cause of a problem, failure of the coating within a corrosive environment, MFL corrosion surveys only find the result of the problem, corrosion defects that may permanently alter the pressure carrying capacity of the pipeline. Stress corrosion cracking (SCC) can be detected using in-line inspection (ILI) technology, but the availability of tools is limited and the cost of inspection is high compared to MFL inspection. SCC almost always occurs at coating faults; direct coating assessment could indicate future problems that could degrade the serviceability of the pipeline.

In this project, a new sensor was developed to assess external coating that could work with currently available ILI tools for minimal additional cost to perform the inspection. The sensors, electromagnetic acoustic transducers (EMATs), generate ultrasonic waves that are guided by the pipe material around the circumference of the pipe. The coating material and adherence can influence the propagation of the ultrasonic waves; changes in ultrasonic signal features were attributed to coating faults. This development used modeling and experiments to establish a more optimal configuration for coating assessment. A multiple feature approach was used.

A commonly used feature, signal amplitude, provided good sensitivity to coating condition but was influenced by inspection variables. One unique feature identified in this development is arrival time of the ultrasonic wave. For the wave type and frequency selected, the wave velocity was different for bare and coated pipe. Therefore, debonded or missing coating can be detected by monitoring arrival time of the ultrasonic wave, a feature that is amplitude independent. Another feature for assessing coating, absorption of selective frequencies, was also demonstrated.

Coating assessment capability was experimentally demonstrated using a prototype EMAT ILI tool. All three detection features were shown to perform well in an ILI environment as demonstrated at Battelle's Pipeline Simulation Facility and BJ Inspection Services pull rigs. Improvement to the prototype occurred between each test; the most significant improvement was the design and construction of a novel set of thick-trace transmitting and receiving Printed Circuit Board (PCB) EMAT coils. Implementation variables such as moisture and soil loading were shown to have a minimal influence on results.

The project team was comprised of the Department of Transportation (DOT), Pipeline Research Council International (PRCI), BJ Inspection Services, Battelle, and FBS Inc.

Executive Summary

Coatings used to protect oil and natural gas pipelines can degrade over time, enabling corrosion and stress corrosion cracks to initiate and grow. Pipeline companies use inline inspection (ILI) tools to detect these anomalies and repair methods to mitigate the result of a failed coating. This project developed inspection sensors that could prevent these anomalies from occurring in the first place by monitoring the integrity of the external protective coating of the pipeline. This coating assessment could be performed during typical ILI that will help pipeline owners assess the general health of the coating protecting their pipeline system. A goal of the design was to keep these sensors simple so that an implementation would not add substantial cost or complexity to a typical magnetic flux leakage (MFL) or caliper survey.

In this development, a sensor system was designed to generate the proper wave type and modes to assess coating conditions. Non-contact electromagnetic acoustic transducers (EMATs) were designed to send guided waves around the circumference of the pipe. With the use of guided ultrasonic waves, as opposed to bulk wave ultrasound, very few ultrasonic sensors were required for implementation. For pipes less than 20 inches in diameter, only two are required: one for sending the wave and a second for receiving. For larger diameter pipes, four EMATs were used for 100-percent circumferential coverage, two EMATs reserved for the excitation of ultrasonic energy and the remaining two reserved for receiving the signal. This number of EMATs is an entire order of magnitude less than the number of bulk wave ultrasonic transducers that would be required to obtain only partial circumferential coverage.

Coating assessment capability was experimentally demonstrated using a prototype EMAT ILI tool. All three detection features were shown to perform well in an ILI environment. These demonstrations occurred in Pull Rigs at Battelle's Pipeline Simulation Facility and BJ Inspection Services. Improvement to the prototype occurred between each test; the most significant improvement was the design and construction of a novel set of thick-trace transmitting and receiving Printed Circuit Board (PCB) EMAT coils. These coils were designed very specially to be capable of handling the high current densities created by the 1200V amplifier. Implementation variables such as moisture and soil loading were shown to have a minimal influence on results.

Coating assessment using ultrasonic waves is not entirely new. Ultrasonic pigs designed to detect stress corrosion cracks are often influenced by coating condition. Most ultrasonic-based SCC tools are typically good coating detection tools and sometimes marketed for this application. However, the implementation is typically complex with the number of sensors and wave properties chosen to detect and size small cracks. In contrast, this development was focused on developing a coating assessment tool, with modeling and experiments to establish a more optimal configuration for coating assessment. The result of this approach was the fundamental improvement over existing methods. The most common approach to assessing coating condition is to assess the amplitude of the received signal; low amplitude means that the coating is good because the ultrasonic energy went into the coating and was absorbed while high signal amplitude means that coating was not intact. While this works reasonably well, the pitfall in this approach rests with the fact that the amplitude is affected by many inspection variables including surface roughness, pig speed, and debris. By taking a more fundamental approach to the design, new features for assessing coating were established. One unique feature identified in this development is arrival time of the ultrasonic wave. For the wave type and frequency

selected, the wave velocity is different for bare and coated pipe. Therefore, disbanded or missing coating can be detected by monitoring arrival time of the ultrasonic wave, a feature that is amplitude independent. Another feature for assessing coating, absorption of selective frequencies, was also demonstrated.

Along with the benefit of knowing coating condition, this technology could help justify longer reinspection intervals for corrosion surveys. For lines with a few manageable corrosion anomalies as demonstrated by a MFL survey, verifying that the protective coating is intact would help justify that the threat is properly addressed. An additional benefit would be improved assessment of the stress corrosion cracking (SCC) threat. One method to assess whether SCC is present on a pipeline is to conduct bell hole excavations. The excavations are sometimes focused by soil modeling to establish that susceptible environment is present. The coating assessment results available from this new technology could be used to focus digs at locations with coating faults. Fewer excavations could be performed to establish the viability of the threat.

The project team was comprised of the Department of Transportation (DOT), Pipeline Research Council International (PRCI), BJ Inspection Services, Battelle, and FBS Inc.

This page intentionally blank.

Table of Contents

	Page
Public Abstract.....	iii
Executive Summary	iv
1.0 Introduction.....	1
1.1. Motivation	1
1.2. Literature Review	1
1.3. Overview of Work.....	2
2.0 Analytical Modeling of Circumferential Guided Waves	4
3.0 Numerical Modeling of Circumferential Guided Waves.....	12
4.0 Experimental Proof of Concept	17
5.0 Sensor and Hardware Design.....	28
5.1. Sensor Design.....	28
5.2. Hardware and Software Design.....	37
6.0 Results of Pull Tests.....	41
6.1. Round 1: Battelle PSF, West Jefferson, OH	41
6.2. Round 2: Battelle PSF, West Jefferson, OH	48
6.3. Round 3: BJ Services, Calgary, AB, CA.....	50
6.4. Inspection Variables.....	54
7.0 Conclusion and Future Direction	55
8.0 References.....	57

List of Figures

Figure 2-1. SH wave (top) and Lamb-type wave (bottom) dispersion curves for a 24 in. diameter, 0.22 in. thick pipe with a 1 mm polymer wrap coating.....	5
Figure 2-2. SH wave (top) and Lamb-type wave (bottom) dispersion curves for a 24 in. diameter, 0.22 in. thick pipe with a 1 mm epoxy coating.....	6
Figure 2-3. Wave structures for the SH ₀ mode for a 130 kHz wave traveling in a pipe with a 1 mm polymer wrap coating (left) and for a 300 kHz wave traveling in a pipe with a 1 mm epoxy coating (right).....	7
Figure 2-4. Measured longitudinal bulk-wave attenuation trends for a Fibrous Coal Tar coating (a) and a Fusion Bonded Epoxy coating (b)..	8
Figure 2-5. Phase (a) and group (b) velocity dispersion curves for a 24-in. diameter schedule 10 pipe with a 3-mm thick coal-tar wrap coating.....	9

Figure 2-6. Particle displacement and shear stress distributions for (a) SH0 at 30 kHz, (b) SH1 at 130 kHz, and (c) SH2 at 312 kHz.	10
Figure 2-7. SH-wave attenuation dispersion curve for the SH0 mode in a pipe 24 in. diameter pipe with a coal-tar enamel coating.	11
Figure 3-1. Cross-sectional view of 130 kHz SH-wave traveling in an 8-in. diameter coal-tar coated pipe with an aspect ratio of 0.94.	13
Figure 3-2. Oblique view of 130 kHz SH-wave traveling in an 8-in. diameter bare pipe with an aspect ratio of 0.94.	13
Figure 3-3. RF waveforms showing comparison between 130 kHz SH-wave traveling in a bare pipe (blue) and in a pipe with a 3-mm coal-tar enamel coating (magenta).	14
Figure 3-4. 2D FEM of Lamb wave propagation in a 24-in. schedule 40 pipe with a 2.5-mm tar coating.	14
Figure 3-5. 2D FEM of Lamb wave propagation in a 24-in. schedule 40 pipe with a 2.5-mm tar coating.	15
Figure 3-6. 3D FEM of wave propagation along the axis of a pipe with a disbonded coating region.	15
Figure 3-7. RF waveforms obtained from FEM of 50 kHz axial L(0,2) wave in 12-in. schedule 40 pipe.	16
Figure 4-1. Lorentz EMAT transducer principle.	17
Figure 4-2. Lamb wave EMAT transducer.	18
Figure 4-3. SH wave EMAT transducer.	18
Figure 4-4. (a) Dual-layer EMAT racetrack coil and (b) Neodymium Rare-Earth magnet array.	19
Figure 4-5. Sensor configuration which allows for the normalization of the received circumferential pulses.	20
Figure 4-6. Ultrasonic waveforms obtained from a 20-in. diameter schedule 10 pipe with a coal-tar enamel coating with a (a) bare pipe, (b) 2-ft. disbond, and for a (c) 1-ft. disbond.	21
Figure 4-7. STFTs of RF-waveforms for a (a) 1ft disbond, (b) 2ft disbond, and for a (c) bare pipe.	22
Figure 4-8. A plot showing the time, frequency, and amplitude disbond detection features for three different disbond sizes in a coal-tar enamel coated pipe.	22
Figure 4-9. Angular group velocity dispersion curve for the SH0 mode in a 24-in. diameter pipe for various coal-tar mastic coating thicknesses.	23
Figure 4-10. Experimental setup used to study the effect of coating thickness on the propagation of a 130 kHz SH-wave.	23
Figure 4-11. Analytic envelopes of the directly transmitted wave packet showing amplitude reduction and time-shifting with increasing coating thickness.	24

Figure 4-12. Plots showing the time-of-flight and amplitude change as coating thickness is increased.	24
Figure 4-13. Photographs of a 20-in. pipe with a coal-tar coating. (a) disbond with a “clean” interface, (b) disbond with a clay/sand earth mixture present at interface, (c) disbond with pottery clay present at interface.	25
Figure 4-14. RF waveforms showing the signal differences for a “clean” disbond (blue), a disbond with clay/sand earth at the interface (green), and a disbond with pottery clay at the interface (red).	26
Figure 4-15. Schematic showing cross-section of soil box.	26
Figure 4-16. Photographs of soil box built for soil loading tests.	27
Figure 4-17. Analytic envelopes of RF waveforms obtained from the disbond regions before (green) and after (red) being buried in compacted soil.	27
Figure 5-1. Pipe-side, tool-side, and cutout views of the EMAT sensor housing package.	29
Figure 5-2. Components of the coil module.	29
Figure 5-3. Mechanical drawing showing recessed EMAT magnet stack and the spring pads (or mechanical springs).	30
Figure 5-4. Photographs showing the assembled EMAT head where (a) shows the nested magnet package, (b) shows the racetrack coil, and (c) shows the PSF test bed vehicle with the EMATs attached.	30
Figure 5-5. Photograph of 2 nd generation sensor carrier and EMAT sensor heads.	31
Figure 5-6. Scanned images of mylar film (left), thick-trace PCB (center), and thin-trace PCB (right) coils.	32
Figure 5-7. Plot showing the received signal amplitude vs. sensor liftoff for the best pulser/receiver combinations.	35
Figure 5-8. Plot showing the received signal amplitude vs. sensor liftoff for the optimal coil combination for both 1000V and 1200V systems.	36
Figure 5-9. System flow chart showing key components.	37
Figure 5-10. Screenshots of waveform display software developed for processing and viewing ILI data.	40
Figure 6-1. Photograph showing four pipes used for pull testing at the PSF.	41
Figure 6-2. Three-dimensional plot of analytic envelopes of ultrasonic data acquired on Pipe 1, which is bare.	43
Figure 6-3. Three-dimensional plot of analytic envelopes of ultrasonic data acquired on Pipe 2, which is coated with a fibrous coal-tar coating.	44
Figure 6-4. Three-dimensional plot of analytic envelopes of ultrasonic data acquired on Pipe 3, which is coated with a wrap coating.	45
Figure 6-5. Three-dimensional plot of analytic envelopes of ultrasonic data acquired on Pipe 4, which had an FBE coating.	46

Figure 6-6. Two-dimensional plot of analytic envelopes of ultrasonic data acquired on Pipe 2 at 1 in. into the pull length (blue) where the pipe was bare and 27 in. into the pull length (red) where an approximate 50-percent circumference disbond existed.	47
Figure 6-7. Short-Time Fourier Transform of ultrasonic data acquired on Pipe 2 at 1 in. into the pull length (left) where the pipe was bare and 27 in. into the pull length (right) where an approximate 50-percent circumference disbond existed.....	47
Figure 6-8. Analytic envelope of the ultrasonic signal obtained in a bare section of pipe.....	49
Figure 6-9. Analytic envelope of the ultrasonic signal obtained in a section of pipe with a disbond in the coal-tar enamel coating.	49
Figure 6-10. RF waveform obtained during a pull through a bare pipe at a speed of approximately 4mph.	50
Figure 6-11. Photograph of pull rig at BJ Services’ facility in Calgary, AB, CA.	51
Figure 6-12. Photograph of prototype ILI tool showing sensor carriage (in pipe) and electronics carriage (on stage).....	51
Figure 6-13. RF waveforms from two channels obtained during a hand-pull through a bare pipe specimen at BJ Services’ facility.	52
Figure 6-14. RF waveforms from several random locations obtained during pull tests through BJ Services’ pull rig.	53
Figure 6-15. RF waveforms from two channels obtained during a hand-pull through a bare pipe specimen at BJ Services’ facility.	54

List of Tables

Table 2-1. Measured parameters and acoustic properties of coatings applied to the 24-in. schedule 40 pipe specimens provided by Battelle for FBS, Inc.	8
Table 2-2. Material properties and dimensions used for dispersion curve generation.	10
Table 4-1. Illustration and table showing desired wavelength and magnet dimensions to generate 130 kHz SH0 mode in a bare pipe.	19
Table 5-1. Specifications of different EMAT coils used in performance evaluation	32
Table 5-2. Specifications of arbitrary waveform generator.	38
Table 5-3. Specifications of A/D card.	38
Table 5-4. Specifications of digital counter.	39
Table 5-5. Specifications of 1200V amplifier.....	39
Table 6-1. Description of pipe samples used for pull tests at the PSF.....	41
Table 6-2. Summary of disbond detection results for several pull locations for Pipe 2 (Fibrous Coal-Tar Coating).	48

1.0 Introduction

1.1. Motivation

A majority of all buried pipeline are coated with protective materials to prevent damage during the installation process and, more importantly, to insulate the pipe from the surrounding corrosive environment. If the coating becomes disbonded, condensation and oxygen will accrue in the disbonded area. Because the coating is still present, but disbonded, it may insulate the metal under the disbond from the cathodic protection, causing that portion of the pipe to corrode more rapidly than if it was in direct contact with the surrounding soil.

For this and other reasons, pipelines are inspected for metal-loss defects using Magnetic-Flux Leakage (MFL) In-Line Inspection (ILI) tools. Because MFL ILI depends on the ferrous nature of the material being inspected, it is only capable of detecting the effect of the corrosion problem and not the cause, a failure of the protective coating. Coating holiday detection techniques, such as the Direct Current Voltage Gradient and Close Interval Potential Survey methods, require the pipe metal to be in direct contact with the surrounding soil and, therefore, are also not always capable of detecting disbonds. The ability to detect coating disbonds in a reliable robust fashion would represent a significant contribution to the pipeline integrity management sector, as it would enable preventative maintenance action prior to the development of corrosive metal-loss defects.

1.2. Literature Review

Sending the ultrasonic energy in the circumferential is a natural and practical approach to assessing coating condition in pipelines. However, compared to the body of work relating to wave propagation in the axial direction of hollow cylinders, the work regarding the propagation of circumferential waves is relatively terse. Viktorov [1] first addressed the topic of Lamb-type wave propagation in the circumferential direction of a circular annulus. He defined the concept of angular wave number, which is a unique physical phenomenon of guided waves traveling in curved space. Qu [2] and Lui [3] presented numerical solutions of the dispersion equation and displacement profiles for circumferential Lamb-type waves. Chapter 12 of Rose [4] also addresses this topic. Lui [5] studied transient circumferential wave propagation using the Normal Mode Expansion technique. Li [6] used the work of Lui [5] to determine the optimal angle-of-incidence for the detection of radial cracking on the inner surface of an annulus. Valle [7] also studied radial crack detection and sizing using Lamb-type circumferential waves. Valle [8] addressed the propagation of circumferential Lamb-type waves in a solid shaft within a single cylindrical layer but because of the highly specialized structural geometry and boundary and interfacial continuity conditions, the presented solution is not applicable to multilayered hollow cylinders. Towfighi [9] and Jiandong [10] used Fourier series and Legendre polynomials, respectively, to solve the coupled governing differential equations encountered for circumferential Lamb-type wave propagation in single-layered anisotropic media. Of particular interest to this study is the work completed by Zhao and Rose [11] on the propagation of circumferential shear-horizontal (SH) waves in an isotropic annulus. This is the first treatment of circumferential SH-wave propagation. The dispersion relation and wave structures are derived

analytically and phase velocity dispersion curves and wave structures are compared to that of a flat plate.

In addition to the cited refereed journal publications, there have been several industrial research projects that have addressed topics similar to that of the present work. Nestleroth and Alers [12] were the first to study the topic of missing and disbonded coating detection using guided waves implemented with ILI tools. In their work, Electromagnetic Acoustic Transducers (EMATs) were employed using the magnetic field present from an MFL tool to generate guided Lamb-type waves, which propagated along the axial direction of the pipe. Signal amplitude was the single discretionary feature for missing and disbonded coating detection. Missing and disbonded coating detection was realized but it was determined that other detection features were needed for a more reliable inspection. Also, the technique did not work as well for thinner coatings such as Fusion Bonded Epoxies (FBEs).

Aaron [13] studied the detection and sizing of stress corrosion cracking (SCC) using EMATs deployed from an ILI tool. A Magnetostrictive EMAT technique was employed to generate circumferentially traveling SH and Shear-Vertical (SV) guided waves. A bench scale ILI tool was constructed and used to perform sizing studies on SCC. Coating disbondment was not addressed. Al-Qahtani [14] demonstrated a fully operational EMAT tool for the detection of SCC and coating disbondment detection. A SH-wave technique was employed but, as was the case in the work done by Nestleroth and Alers [12], signal amplitude was the only contrast mechanism used for coating disbondment detection.

Over the past several years, several industrial ILI vendors, such as Rosen Inspection Technologies and General Electric, have introduced coating assessment services/tools. One thing that all these technologies have in common is that they use only signal amplitude to detect coating problems. In most cases, the coating assessment capability of the tool is simply a byproduct of a tool designed for SCC detection. The primary objective of this work is the theoretically-driven design of a multiple-feature coating failure detection routine that is both more reliable and robust than the state-of-the-art technologies; in short, a tool that is designed specifically for coating assessment. This task is accomplished through the theoretical analysis of the circumferential guided wave dispersion curves and wave structures, which many of the previous works have not done thoroughly if at all.

1.3. Overview of Work

Section 2 of this report addresses the theoretical studies that were completed as a result of this work. Dispersion curves are presented for both Lamb-type waves and SH-waves and a logical argument is presented for the use of the fundamental SH-wave mode for the detection of coating disbonds. Wave structures and other supporting materials are presented. Several potential disbond detection features are proposed.

Section 3 presents the results of some numerical modeling that was performed to demonstrate the validity of the coating assessment features proposed in Section 2. A bare pipe model is compared to a coated pipe model and the differences in the results are highlighted. The properties used in the modeling were obtained from direct measurement of a coating sample presented in this section.

Section 4 presents the proof-of-concept studies performed to demonstrate the sensitivity of the coating assessment features that were introduced in Section 2 and to explore the practical implementation of a system capable of making the necessary measurements. Experimental studies were completed on pipe with coal-tar enamel coatings as it has been suggested that they are the most likely type to develop disbonds and general failures.

Section 5 presents the design and construction of a prototype ILI tool for coating assessment. Several of the key design features are discussed. The supporting hardware and software are also discussed.

The results from several rounds of pull-tests are presented in Section 6. The pull-tests were completed at Battelle's Pipeline Simulation Facility (PSF) in West Jefferson, OH and at BJ Service's pull facility in Calgary, AB, CA.

Section 7 summarizes the key findings and contributions of this work and presents some directions for future work.

2.0 Analytical Modeling of Circumferential Guided Waves

Theoretical and numerical modeling are invaluable tools as they can be used to predict the expected behavior of ultrasonic waves propagating in a bounded structure. By comparing this expected behavior with the behavior observed by experiment, it is possible to correlate certain features to structural variations such as coating presence and integrity. To aid in the selection of guided wave modes and frequencies that would be sensitive to coating presence, or lack thereof, several desired wave properties were defined. An acceptable mode/frequency for coating assessment should adhere to the following characteristics:

- The selected modes/frequencies **should** be affected by the presence, or lack of presence, of coating in more than one way (e.g. attenuation, velocity, frequency, etc.).
 - Modes exhibiting velocity variation due to coating presence will provide a time-based characterization feature.
 - While all modes are attenuated by coating, modes with moderate attenuation must be selected over modes exhibiting excessive attenuation or too little attenuation. This will provide an amplitude-based characterization feature.
 - Modes whose attenuation varies moderately with frequency will illustrate a frequency filtering effect and will therefore provide a frequency-based characterization feature.
- The selected modes/frequencies **should not** be sensitive to variations in pipe wall thickness.
 - By choosing a mode/frequency whose velocity varies with coating presence, but not with wall thickness, it will be possible to design a sensor that can be used on multiple pipe sizes.
 - Selecting this type of mode will also prevent the confusion of corrosion areas with areas of disbanded or missing coating.
- The selected modes/frequencies **should not** mistake a wet interface for well-bonded coating.
 - To avoid confusing water with well-bonded coating, a mode with completely in-plane or dominantly in-plane displacement must be selected.
- The final dimensions and specifications of the sensors needed to generate the selected modes/frequencies must conform to the limitations imposed by the ILI tool and environment.
 - EMATs must work reliably, even with small fluctuations in sensor liftoff. This is accomplished by using strong magnets, high excitation voltages, and as low a frequency as possible, although, very low frequency EMATs have a large footprint and will be avoided.

With these desirable properties in mind, the development of the theoretical modeling tools necessary to characterize guided-wave propagation in the circumferential direction of a pipe was

completed. A significant result of this effort has been the development of a multilayer circumferential guided-wave dispersion curve code. Both SH wave and Lamb-type wave codes have been developed. In addition, computer codes have been developed to compute the wave structure of any desired mode/frequency combination for both types of waves. Figure 2-1 and Figure 2-2 show the SH- and Lamb-type dispersion curves for a polymer wrap and epoxy coating, respectively. In each plot, the black solid line corresponds to the bare pipe case while the red solid line corresponds to the coated pipe case.

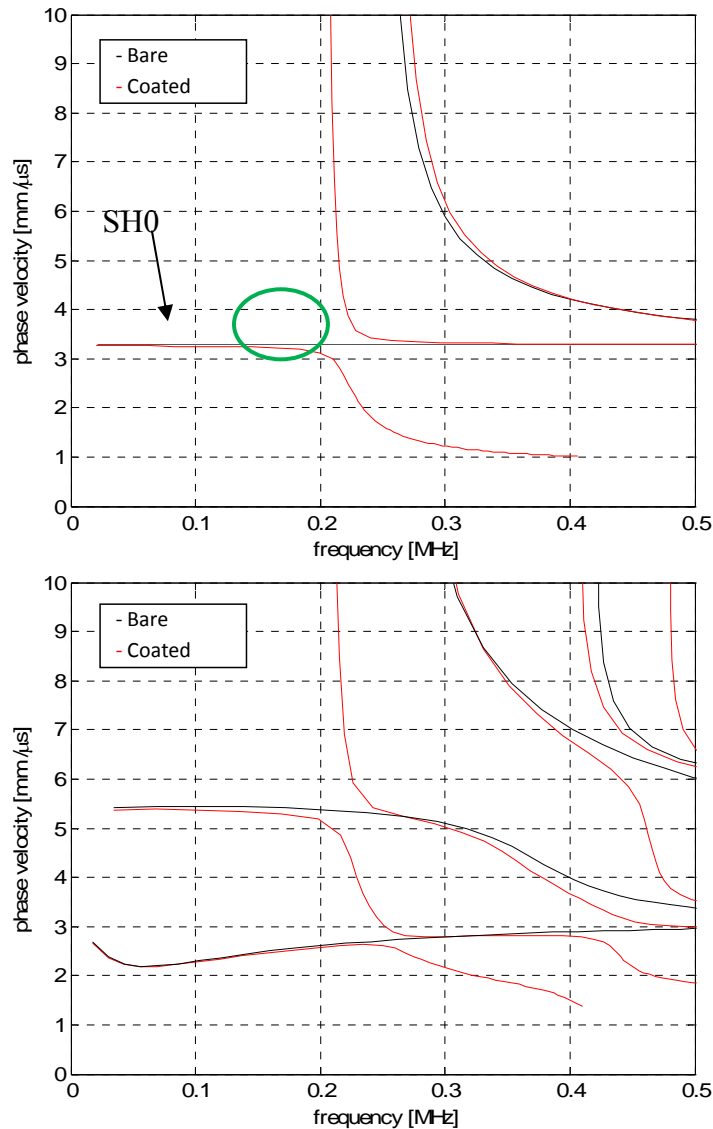


Figure 2-1. SH wave (top) and Lamb-type wave (bottom) dispersion curves for a 24 in. diameter, 0.22 in. thick pipe with a 1 mm polymer wrap coating. Black curves represent the bare pipe case and the red lines show the curves for the pipe with the polymer wrap coating. The green circle indicates the optimal excitation region.

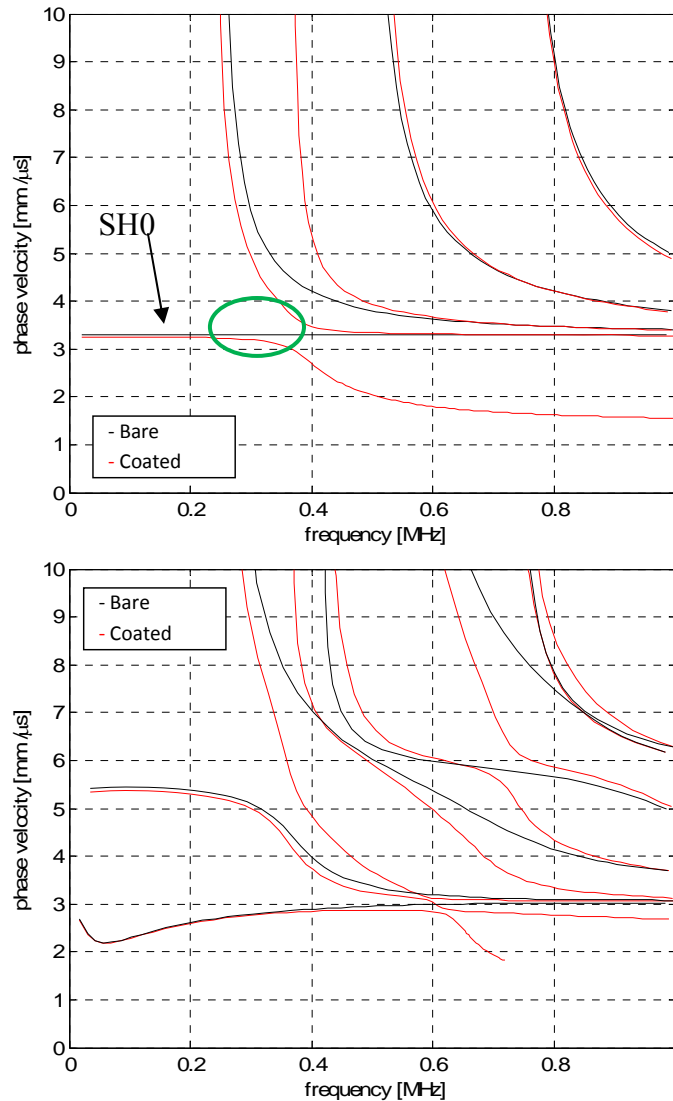


Figure 2-2. SH wave (top) and Lamb-type wave (bottom) dispersion curves for a 24 in. diameter, 0.22 in. thick pipe with a 1 mm epoxy coating. Black curves represent the bare pipe case and the red lines show the curves for the pipe with the epoxy coating. The green circle indicates the optimal excitation region.

Based on the analysis of the dispersion curves using the above-mentioned criteria, it was determined that the SH0-like modes were optimal candidates for the detection of disbonded or missing coating. For bare pipe, this mode is completely non-dispersive with a constant phase velocity of 3.23 mm/μs for all wall thicknesses. Therefore, it is not highly sensitive to variations in wall thickness. When a lower acoustic impedance coating is introduced, such as coal-tar enamel or epoxy, the phase velocity drops by a noticeable amount. This velocity difference can be used as a time-based feature for disbond or missing coating detection.

The green circles in the top plots of Figure 2-1 and Figure 2-2 indicate the optimal excitation regions of the SH modes for coating assessment of the respective coating types and thicknesses. This region is chosen because the change in velocity is large enough to be measured yet frequency is still relatively low, minimizing attenuation of the guided wave. Higher frequencies

may require multiple sensor pairs to obtain full circumferential coverage. It is seen in Figure 2-2 that, for epoxy-like coatings, higher frequencies are required to resolve the velocity difference between the bare and coated cases. This is acceptable since epoxy coatings are also less attenuative than bituminous and rubber-based coatings.

Another highly desirable feature of SH-waves is that particle displacement is completely in-plane and therefore energy will not leak into disbonds filled with water. Figure 2-3 shows the wave structures for the SH0 mode at 130 kHz for a pipe coated with polymer wrap and at 300 kHz for a pipe coated with epoxy. It is seen that both wave structures have significant displacement and maximum shear stress at the pipe/coating interface.

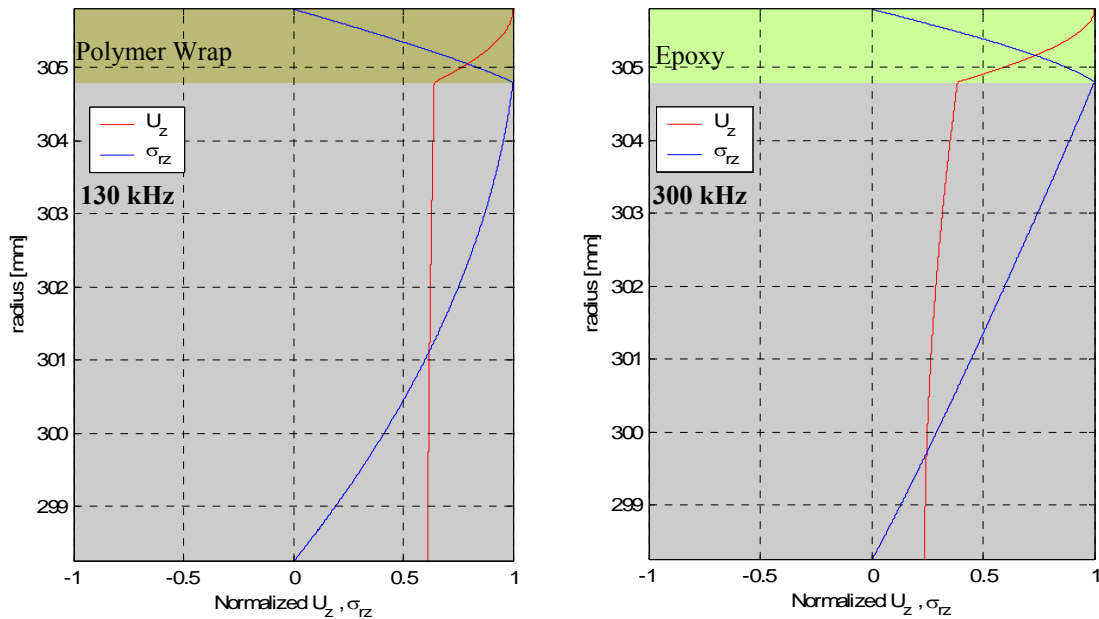
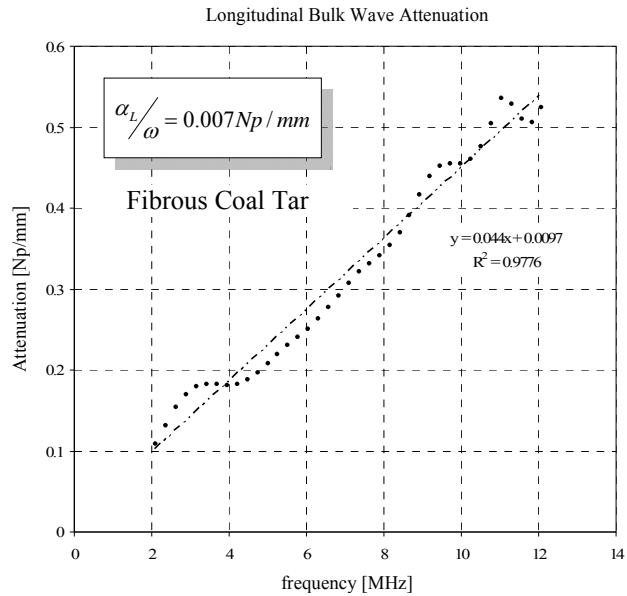


Figure 2-3. Wave structures for the SH0 mode for a 130 kHz wave traveling in a pipe with a 1 mm polymer wrap coating (left) and for a 300 kHz wave traveling in a pipe with a 1 mm epoxy coating (right).

In the early stages of the project it was determined that the concentration of the research effort should be on coal-tar enamel coatings as they have a strong case history for failure. Battelle subsequently provided FBS, Inc. with a 24 in. diameter pipe specimen coated with a coal-tar enamel coating. A Fusion Bonded Epoxy (FBE) specimen was also provided. FBS Inc. used its proprietary VECTOR coating assessment technology to measure such things as coating thickness, density, wave velocity, and bulk-wave attenuation. Figure 2-4 shows the bulk-wave attenuation measurement results for the (a) fibrous coal-tar enamel and (b) FBE coatings. Table 2.1 summarizes the measured coating properties for each coating.

To select a frequency at which the SH0 mode should be excited to detect disbonds and missing coating in the coal-tar enamel coating, the SH-wave dispersion curves were generated for the approximate material properties and thickness of the specimen provided by Battelle. The bulk shear-wave velocity of the coating was estimated from the measured longitudinal-wave velocity and a Poisson ratio typical of tar-based materials. The phase and group velocity dispersion curves can be seen in Figure 2-5 (a) and (b), respectively. The quantities used in the generation of the curves are summarized in Table 2-2.

(a)



(b)

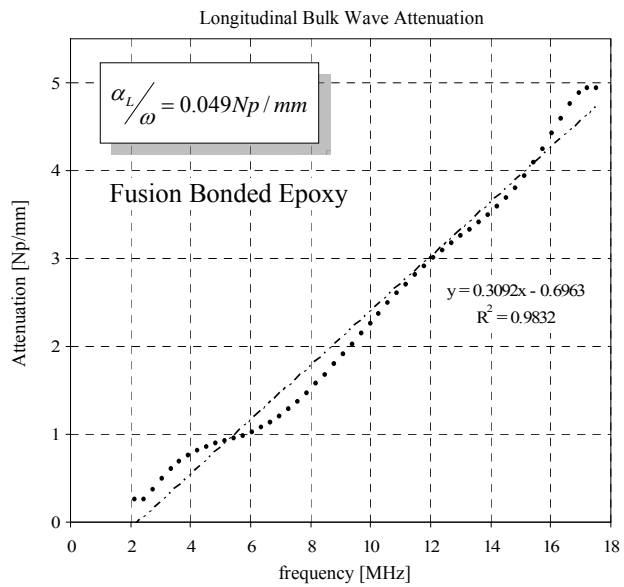


Figure 2-4. Measured longitudinal bulk-wave attenuation trends for a Fibrous Coal Tar coating (a) and a Fusion Bonded Epoxy coating (b). Measured attenuation properties are used to calculate the theoretical attenuation dispersion curves for guided waves.

Table 2-1. Measured parameters and acoustic properties of coatings applied to the 24-in. schedule 40 pipe specimens provided by Battelle for FBS, Inc.

Coating	Thickness (mm)	Density (g/cc)	Longitudinal-Wave Velocity (mm/ μ s)	Longitudinal Bulk-Wave Attenuation (Np / mm \cdot MHz)
Fibrous Coal Tar	3.1	1.5	1.4	0.007
Fusion Bonded Epoxy	0.35	1.25	1.5	0.049

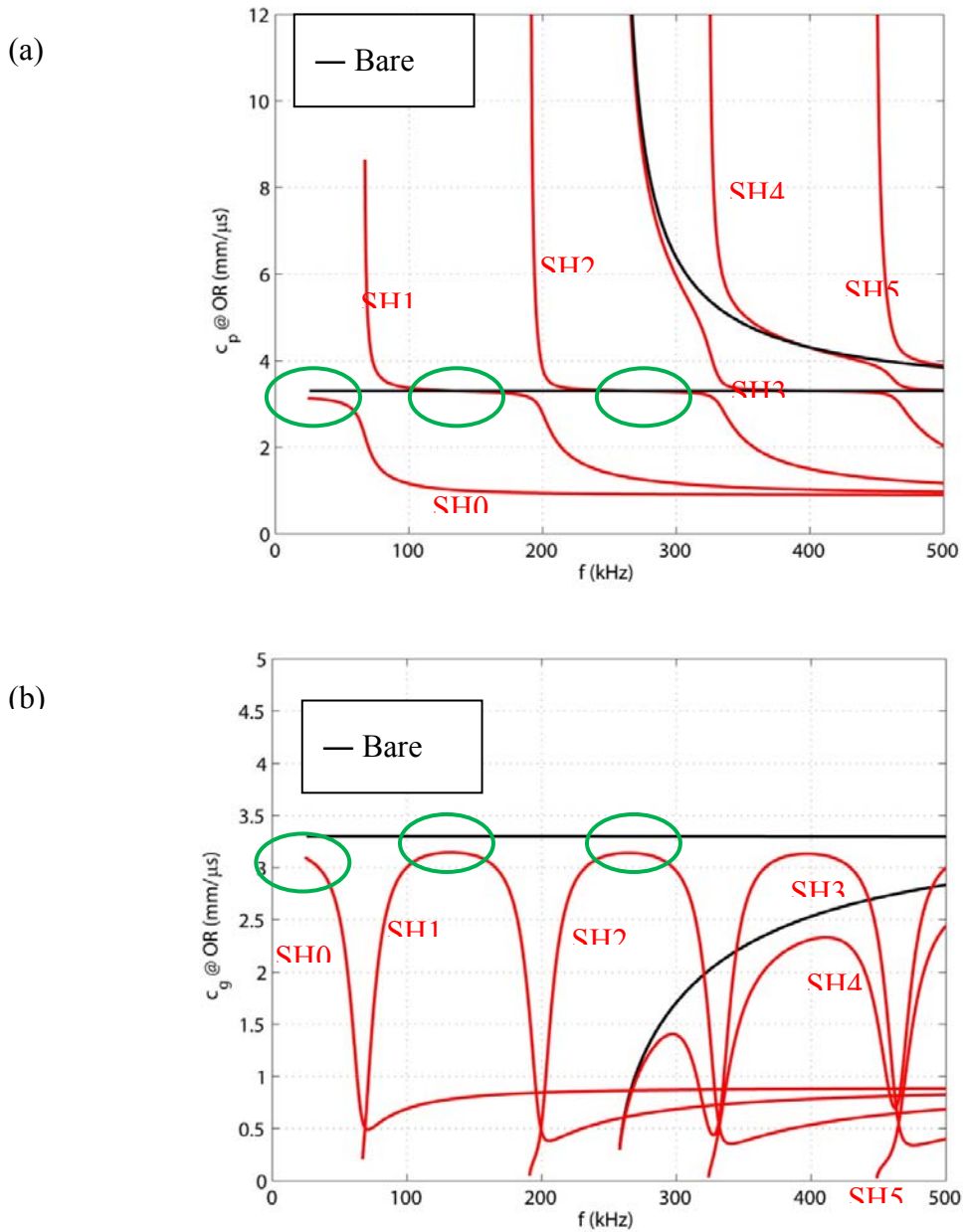


Figure 2-5. Phase (a) and group (b) velocity dispersion curves for a 24-in. diameter schedule 10 pipe with a 3-mm thick coal-tar wrap coating. Black lines correspond to the bare pipe case and are shown for comparison. Green circles indicate optimal excitation regions.

Table 2-2. Material properties and dimensions used for dispersion curve generation.

	Layer 1	Layer 2
Inner Radius (m)	0.24765	0.254
Outer Radius (m)	0.254	0.257
Density (kg/m³)	7930	1500
c_L (m/s)	5920	1400
c_S (m/s)	3260	900

The black lines in both plots of Figure 2-5 correspond to the bare-pipe case and are included for comparison. Based on the aforementioned desirable mode/frequency properties, the phase velocity dispersion curve is examined for a non-dispersive region. The zeroth SH-wave mode, for an uncoated pipe of any thickness and diameter, is completely non-dispersive with a mean phase velocity equivalent to that of the bulk shear velocity. This invariance with thickness satisfies the wall thickness insensitivity criterion. Thus, a relatively non-dispersive coated pipe mode, whose phase velocity approaches that of the bare pipe zeroth mode, will satisfy all the criteria of an ideal mode/frequency. The regions meeting these criteria are indicated by the green circles in Figure 2-5.

The last step is to make sure that the indicated modes/frequencies interact with the coating layer. This is determined from the wave structure plot shown in Figure 2-6 for regions within the green circles. It is seen in this figure that there is both a large particle displacement and shear stress present at the pipe/coating interface, indicating that these particular mode/frequency combinations will be sensitive to the presence of the coating. Large displacements are critical, as this is the quantity measured by the ultrasonic sensors.

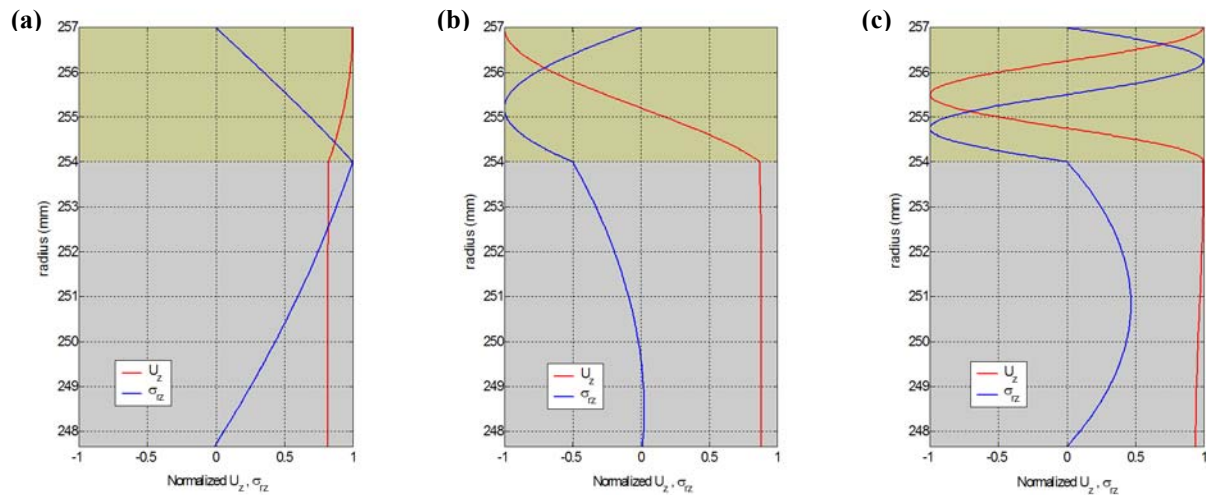


Figure 2-6. Particle displacement and shear stress distributions for (a) SH0 at 30 kHz, (b) SH1 at 130 kHz, and (c) SH2 at 312 kHz.

Because very low frequencies will result in very large sensors, and very high frequencies will result in high attenuation, a compromise must be made between acceptable sensor dimensions and maximum acceptable attenuation. For these two reasons, it was determined that the SH1 mode at a frequency of 130kHz was the optimal mode and frequency for disbond detection in coal-tar enamel coatings of thickness near 3 mm.

With a mode/frequency that meets all predetermined criteria selected, potential disbond detection features were identified. The first, and perhaps most significant, feature followed directly from the consideration of the group velocity dispersion curve shown in Figure 2-5(b). It is seen that the group velocity of the desired mode/frequency is slower for the case of the coated pipe. This implies that the presence and size of a coating disbond will affect the time-of-flight of a circumferential guided wave. This is a non-obvious and significant finding, as time-based features tend to be more reliable than others.

Two more disbond detection features are related to the attenuation of the circumferential guided wave caused by the presence of well-bonded coating. The first, and most obvious and commonly used, feature is a reduction in the amplitude of the traversed wave. A disbond will show as an increase in received wave amplitude as compared to a region of perfectly bonded coating. The second attenuation-related feature is the frequency-dependent attenuation of the propagating wave, as shown in Figure 2-7. For SH-waves, attenuation has an approximately linear increase with frequency and thus it would be expected that higher frequencies would attenuate more quickly than lower frequencies. In other words, a well bonded coating acts as a frequency filter and if a disbond is present, more higher frequency content will be received.

In summary, the theoretical modeling completed in the beginning stages of this project resulted in the identification of several different ideal modes and frequencies for disbond detection and three disbond detection features: one time-based, one frequency-based, and the third amplitude-based. Prior to experimental verification, numerical modeling was used to verify some of the predictions of the analytical modeling. This work is presented in the next section.

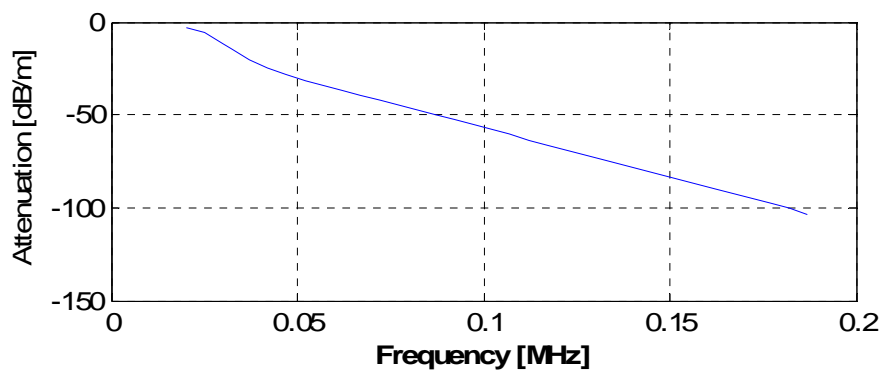


Figure 2-7. SH-wave attenuation dispersion curve for the SH0 mode in a pipe 24 in. diameter pipe with a coal-tar enamel coating.

3.0 Numerical Modeling of Circumferential Guided Waves

Numerical modeling is a very powerful technique that can be used to verify analytical results or to solve problems that are too complex to have closed-form analytical solutions. In this work, numerical modeling was used to verify some of the coating disbond detection conclusions that were drawn from the theoretical analysis. Effectively, numerical modeling is a quick and cost effective virtual experiment that has the added benefit of being free of experimental error.

To verify the trends predicted in Section 1, a finite-element model (FEM) was created. Due to computational limitations, it was not possible to model a 24-in. schedule 10 pipe with a coating layer. In order to overcome this problem, a pipe section with an outer diameter of 8 in. and an inner-to-outer radius ratio of 0.94 was created. For a bare pipe, this is numerically equivalent to the 24-in. diameter pipe. In the model, the dimensions and properties of the coating layer remained the same as in the case of the 24-in. pipe. The excitation source was modeled to imitate the loading achieved using an SH-wave EMAT with a wavelength of 25.4 mm. This loading generated the desired mode when excited at approximately 130 kHz.

A cross section of the pipe at several different times can be seen in Figure 3-1. From these pictures it can be seen that the wave is severely attenuated after just two traversals of the 8 in. diameter pipe. Note that one traversal around a 24-in. diameter pipe is approximately equivalent to three traversals around the 8-in. model, suggesting that the wave would be severely attenuated in one traversal around a 24-in. diameter pipe with the perfectly bonded coal-tar coating. Accordingly, it may be necessary to use multiple sensor pairs for the inspection of larger diameter pipe. Figure 3-2 shows an oblique view of the bare pipe model showing divergence of the wave front.

The resulting RF waveforms of an SH-wave traveling in the circumferential direction of the bare and coated pipe models are shown in Figure 3-3. From Figure 3-3 it can be seen that the time period for one traversal in the coated pipe model is longer than for the bare pipe. The time-of-flight in the 8-in. diameter coated pipe model is 222 μs , corresponding to a velocity of approximately 2.9 mm/ μs , compared to approximately 3.23 mm/ μs for a bare pipe.

Based on the analysis of the FEM presented in Figures 3-1 through 3-3 the velocity and attenuation trends obtained from the model agree with the trends obtained by theoretical analysis. With the numerical and analytical models in agreement the step was to construct a proof-of-concept experiment. This will be the topic of Section 4. But before that work is presented, some other numerical modeling work completed as part of this project will be discussed.

In addition to three-dimensional modeling, two-dimensional modeling was completed for Lamb-type modes. Figure 3-4 and Figure 3-5 show magnified views of a 200 kHz Lamb-type wave mode traveling around a coated pipe. In Figure 3-4 there are two noticeable modes, one symmetric and one antisymmetric mode. The symmetric mode propagates a lower velocity and therefore cannot be seen in Figure 3-5, which was taken just before the waves reached the bottom of the pipe. In Figure 3-4, the green and orange regions are meant to show the relative thickness of the pipe and coating layers. The ending of the delaminated coating area can be seen at the very bottom of Figure 3-5. It is obvious from Figure 3-5 that the presence of a delamination results in decreased attenuation of the clockwise (CW) traveling wave.

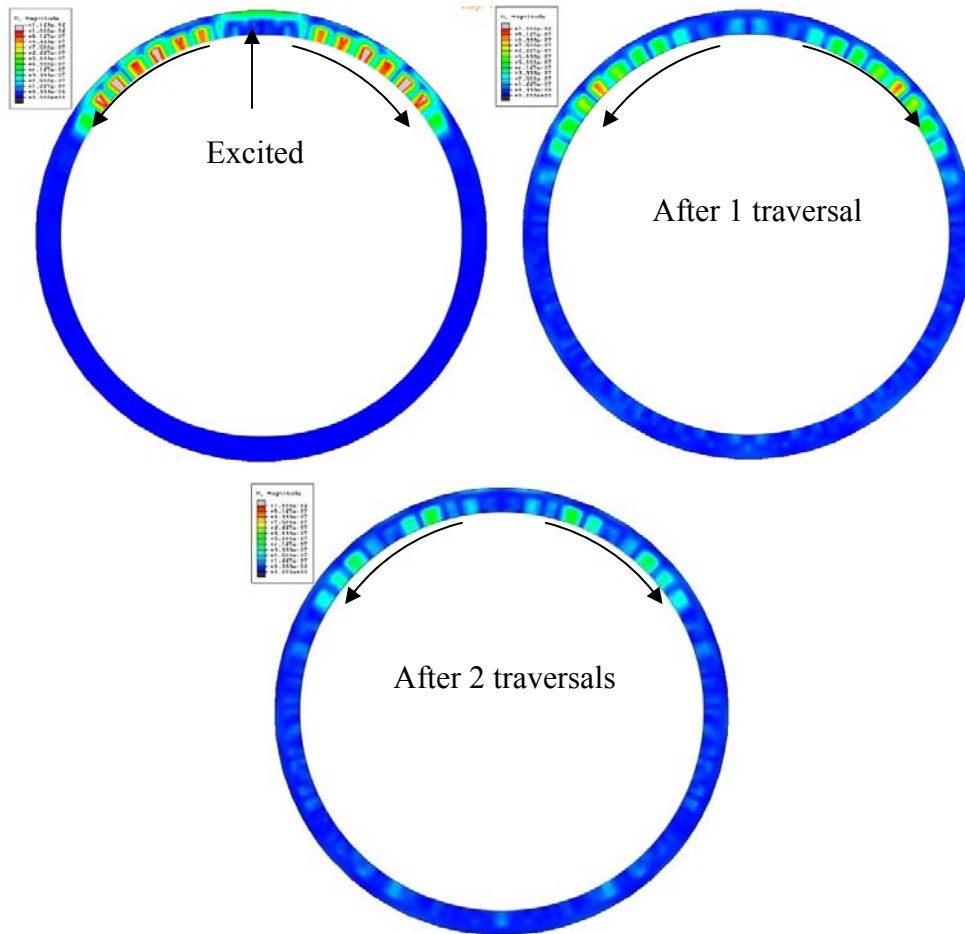


Figure 3-1. Cross-sectional view of 130 kHz SH-wave traveling in an 8-in. diameter coal-tar coated pipe with an aspect ratio of 0.94. Note that one traversal around a 24-in. diameter pipe is approximately equivalent to three traversals around the 8-in. diameter pipe. It is therefore expected that for this mode-frequency combination, the wave would be almost completely attenuated in one traversal around a 24-in. diameter pipe with the perfectly bonded coal-tar coating.

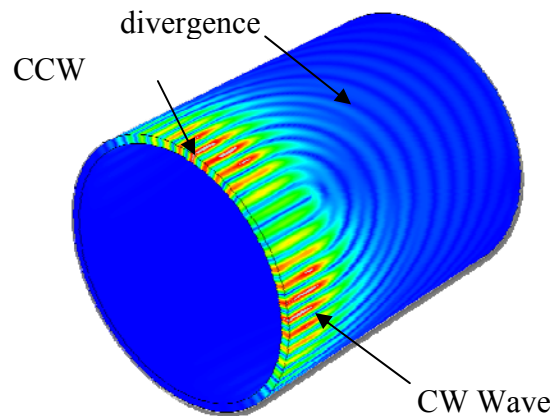


Figure 3-2. Oblique view of 130 kHz SH-wave traveling in an 8-in. diameter bare pipe with an aspect ratio of 0.94. Note that a transverse cut has been made in order to see how the energy is distributed in the pipe wall.

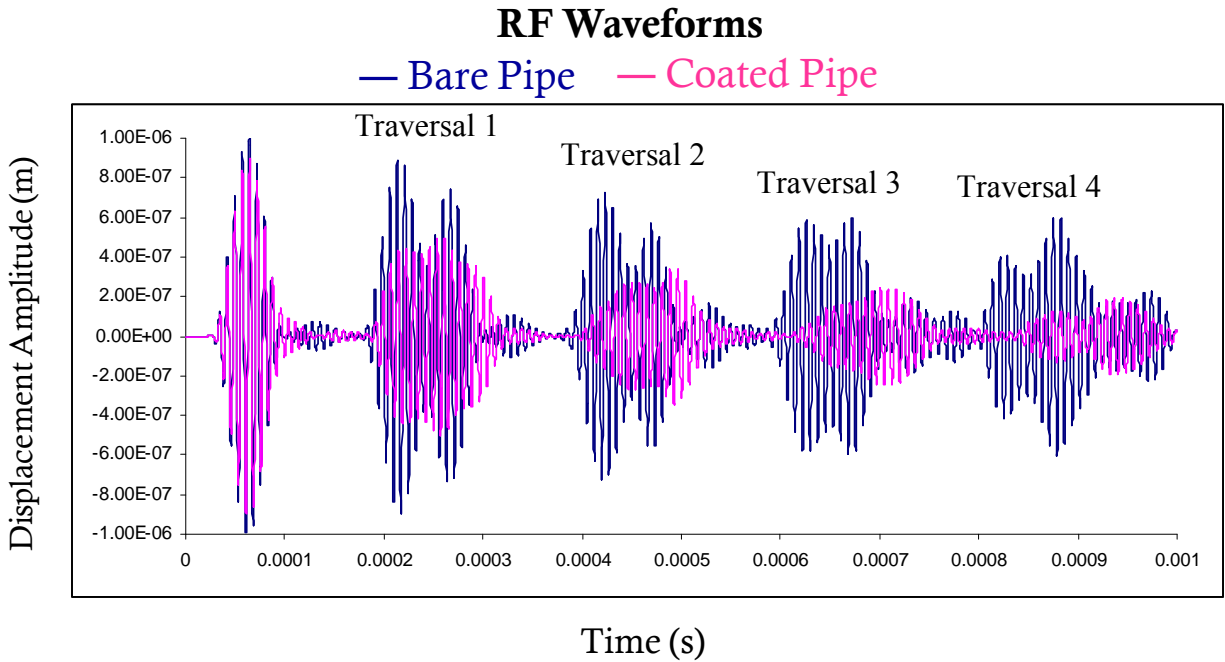


Figure 3-3. RF waveforms showing comparison between 130 kHz SH-wave traveling in a bare pipe (blue) and in a pipe with a 3-mm coal-tar enamel coating (magenta). Two pulses are seen for each traversal because there are waves traveling in both the CW and CCW directions.

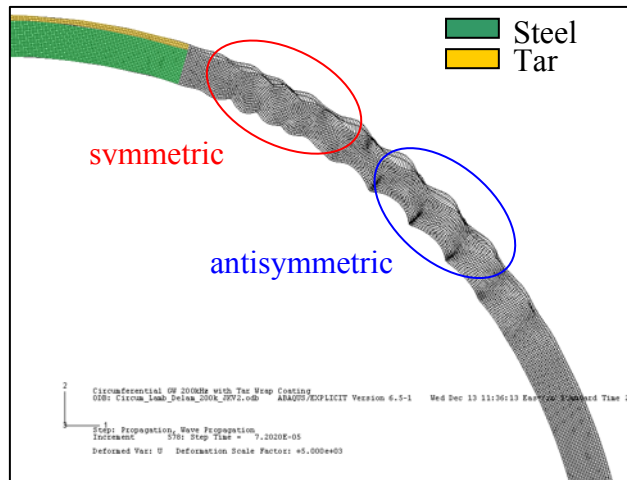


Figure 3-4. 2D FEM of Lamb wave propagation in a 24-in. schedule 40 pipe with a 2.5-mm tar coating. One symmetric mode and one antisymmetric mode are visible. The green and orange regions are only to show the relative thickness of each layer.

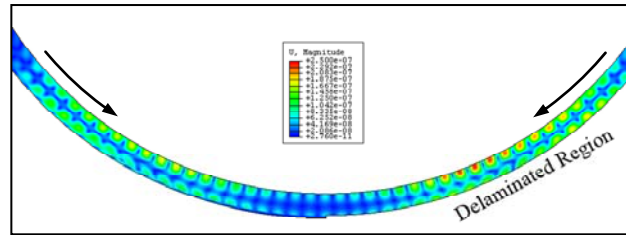


Figure 3-5. 2D FEM of Lamb wave propagation in a 24-in. schedule 40 pipe with a 2.5-mm tar coating. Delaminated region of coating is visible. It is seen that the CCW propagating wave has attenuated more than the CW propagating wave, which is traveling through the delaminated region.

Finally, modeling was completed for guided waves traveling along the axis of the pipe as this sensor orientation also has much potential for implementation with MFL tools. In this case, the disbond was modeled as a 12-in. long, 360° region of missing coating. Figure 3-6 shows an image of the model setup. A fourth potential disbond detection feature is seen in this figure; there is a noticeable reflection from the edge of the delaminated region. This reflection is caused by the sudden change in boundary conditions at this point. There is also a reflection from the end of the delaminated region, though this reflection cannot yet be seen in Figure 3-6 as it is hidden in the saturated region. Figure 3-7 shows the waveforms obtained at the data collection point shown in Figure 3-6. As was seen in Figure 3-3 for circumferential waves, there is a notable time and amplitude shift for the wave that has traveled through the delaminated region. Though the time shift looks small, there is actually a 4- μ s difference, which is significant considering the speeds at which ultrasound travels.

The reflections from the coating boundaries do serve as potential detection mechanisms, though the relative reflection amplitude is quite small. It is expected in practice that, the reflection will be totally absorbed by the coating or otherwise lost in the noise floor prior to reaching the receiving transducer. With this said, it will be verified in Section 4.

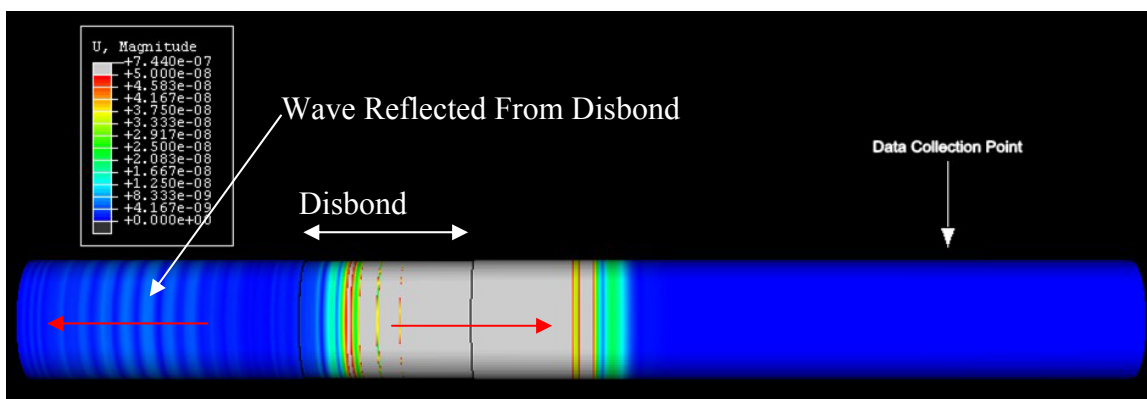


Figure 3-6. 3D FEM of wave propagation along the axis of a pipe with a disbonded coating region. A reflection from the edge of the disbond can be seen traveling back toward the end of the pipe. Excitation was done with the 50 kHz L(0,2) mode.

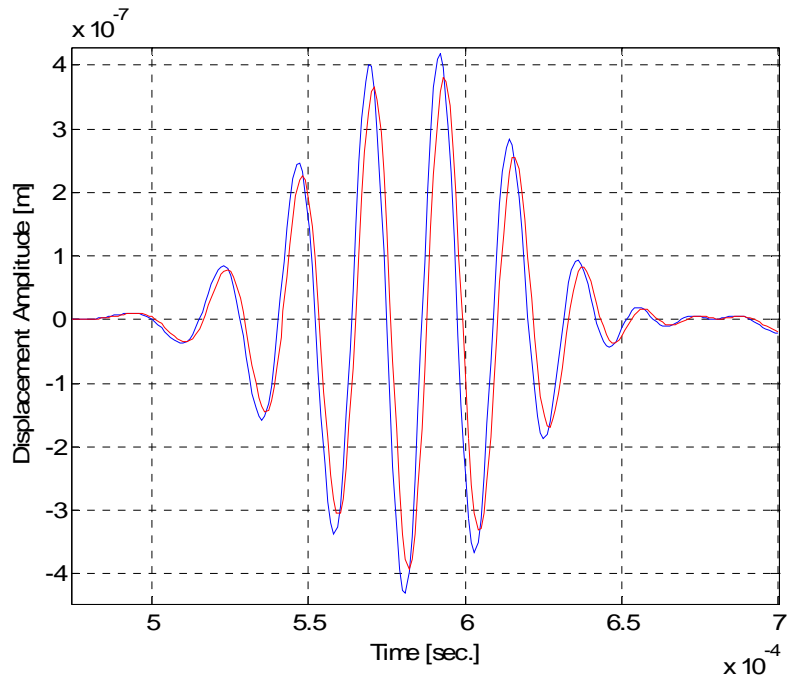


Figure 3-7. RF waveforms obtained from FEM of 50 kHz axial L(0,2) wave in 12-in. schedule 40 pipe. The blue line corresponds to a coated pipe with a disbonded region and the red line corresponds to a coated pipe without any disbonds. In addition to the change in amplitude, there is a 4- μ s difference in the arrival time of the waveforms, which is significant given the speeds at which ultrasound travels.

4.0 Experimental Proof of Concept

In this section, the practicality of the disbond detection features presented in Sections 2 and 3 are explored experimentally. Experiments are performed on a 20-in. diameter pipe with a 3-mm coal-tar enamel coating. Regions of the coating are removed to simulate coating disbonds. A demonstration is also provided for a thin (<1 mm) coal-tar mastic coating. Finally, the effects of soil loading are also explored to determine if soil presence in a disbonded coating area can confound the proposed disbond detection methodology.

For a practical ILI implementation, the sensors should not require any type of coupling liquid and should be capable of efficiently generating SH-waves in the pipe wall. EMATs were determined to be the most appropriate sensor type as they generate and receive ultrasound by coupling magnetic fields to the flow of current within a specimen. EMATs can be non-contact, operate at elevated temperatures, work on rough or oxidized surfaces, and operate at high speeds. Depending on the configuration of the magnetic field and eddy currents, Lamb and SH guided waves can be both generated and received.

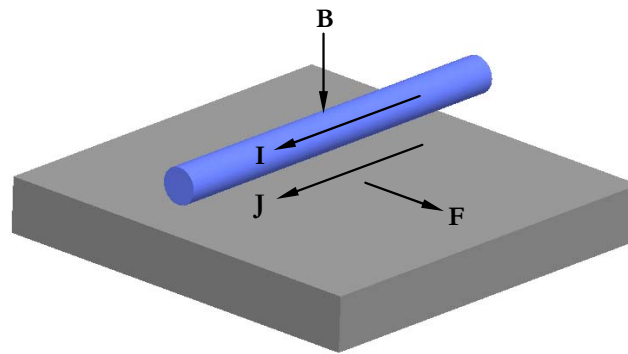


Figure 4-1. Lorentz EMAT transducer principle.

The EMATs used in this project are Lorentz force EMATs. Figure 4-1 illustrates the Lorentz concept. The first component to the Lorentz force transduction mechanism is an eddy current. An eddy current (J) is induced in the part by passing a current (I) through a wire or trace in close proximity to the specimen. The part to be inspected must be conductive for this to occur. In addition to the eddy current, a static magnetic field (B) must be present. When the current is pulsed in the presence of the magnetic field a force (F) is induced in the specimen. The direction of the force can be determined by the right hand rule. The magnitude and direction of the force are given by Equation 1, where F is the force per unit volume, J is the induced dynamic current density, and B is the static magnetic induction.

$$F = J \times B \quad [1]$$

The two most typical Lorentz force EMATs configurations are for the generation of Lamb and SH waves. Figure 4-2 shows the configuration of a Lamb wave EMAT. Lamb wave EMATs generally use what is referred to as a meandering coil with a single large magnet. The wavelength of the induced wave can be altered by changing the spacing between the traces in the

coil. Figure 4-3 shows the typical configuration of an SH wave EMAT. The wavelength of the induced wave for an SH EMAT can be changed by altering the thickness of the magnets. In both the Lamb wave and SH wave EMATs changing the wavelength of the sensor allows the designer to sweep through the dispersion curve space. A given wavelength activates a line on the dispersion curve that originates at the origin, with a given slope. The slope of the line can be altered by changing the spacing. A specific mode can then be activated by exciting the transducer at a set frequency.

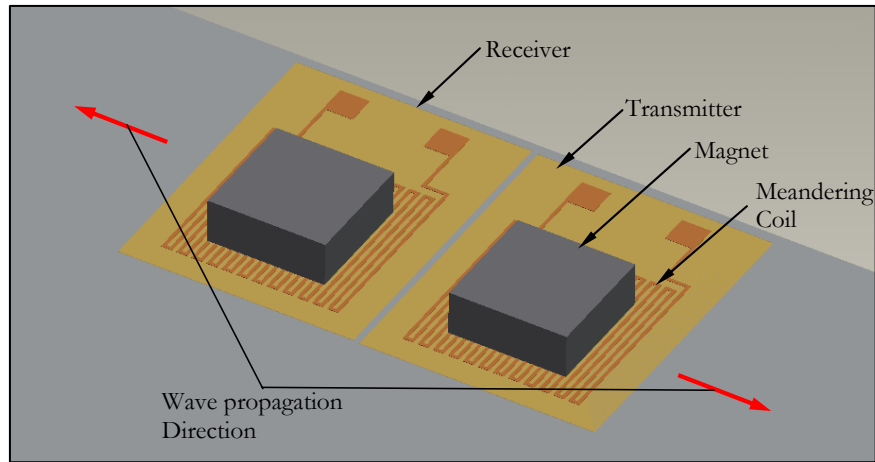


Figure 4-2. Lamb wave EMAT transducer.

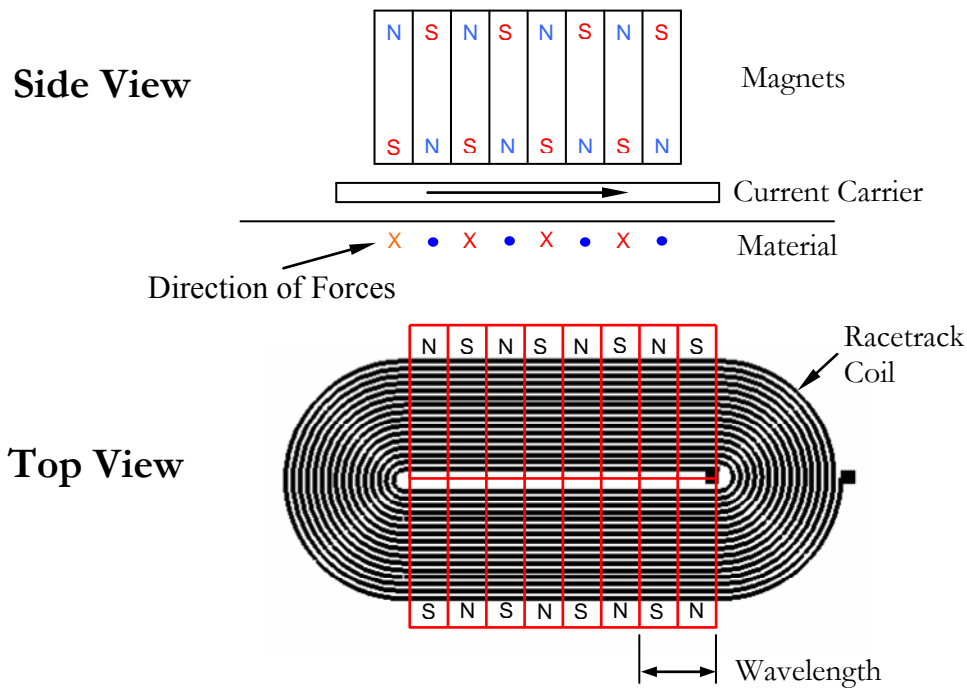
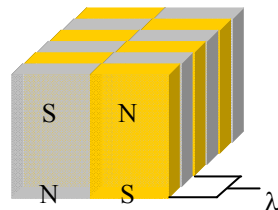


Figure 4-3. SH wave EMAT transducer.

Table 4-1 summarizes the desired wavelengths and corresponding magnet sizes for the 130 kHz SH-wave that was proposed for disbond detection of coal-tar enamels in Sections 2 and 3. The actual dimensions of the obtained magnets are 12.6 mm, resulting in a frequency of 128 kHz. Photographs of the core components of the EMAT components are shown in Figure 4-4. Figure 4-4(a) shows the dual-layer EMAT racetrack coil that was designed specifically for the coating disbond detection task. Figure 4-4(b) shows an array of 80 N-50 grade Neodymium Rare-Earth magnets stacked in 10 columns of 8. The individual magnet dimensions are ½ in.×1 in. ×⅛ in., resulting in a total array height of 1 in. and a sensor wavelength of 25.7 mm.

Table 4-1. Illustration and table showing desired wavelength and magnet dimensions to generate 130 kHz SH0 mode in a bare pipe.



where

$$\lambda = \frac{c_p}{f}$$

EMAT	f (MHz)	c_p (mm/μs)	λ (mm)	Magnet Size (mm)
1	0.13	3.23	24.85	12.42

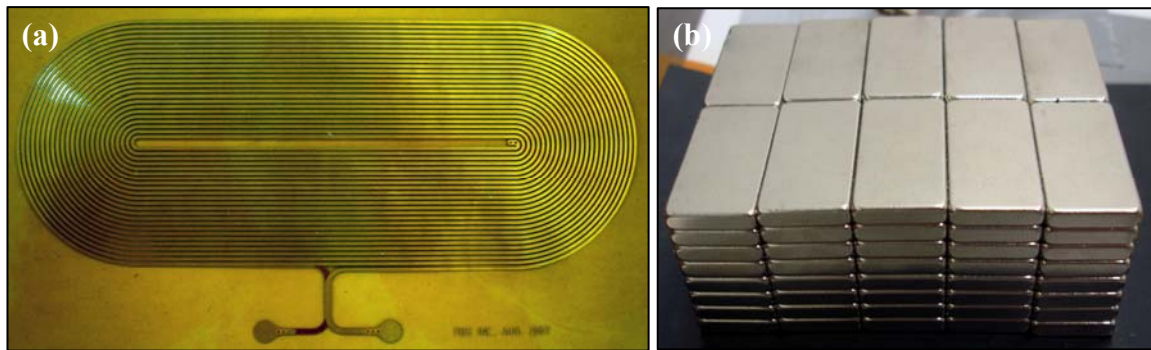


Figure 4-4. (a) Dual-layer EMAT racetrack coil and (b) Neodymium Rare-Earth magnet array.

A sensor configuration was adopted, which will allow for the normalization of all received pulses to an initial reference pulse. An illustration of the sensor configuration is seen in Figure 4-5. In the configuration, the transmitter (T) and receiver (R) are separated by some arc length (ΔS). The reference pulse is the pulse that travels directly from the transmitter to the receiver and its point-of-reception is indicated by the orange dot in the figure. The reference pulse can be used to normalize subsequently received signals in the amplitude, time, and frequency domains. Note that in Figure 4-5, the “green” signal is the first signal to completely traverse the circumference of the pipe, whereas the “red” signal never traverses the area in between the transmitter and receiver prior to first reception. For this reason, the received “green” pulse is the one used to extract information regarding coating integrity.

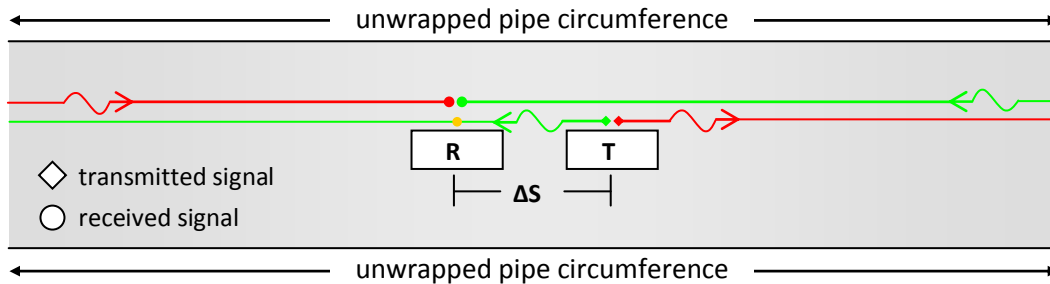


Figure 4-5. Sensor configuration which allows for the normalization of the received circumferential pulses. The received reference pulse (orange dot) is used to normalize the first complete traversal of the pipe circumference (green dot). Note that the “red” pulse has not completely traversed the pipe circumference.

Figure 4-6 shows the results from a coating disbond detection study that was completed using the initial prototype sensor with the sensor configuration described by Figure 4-5. A 20-in. diameter pipe with a coal-tar enamel coating was used for the study. Disbonds were created by removing coating in fixed-size regions. In the figure, the first pulse to complete one traversal of the pipe circumference is compared to the reference pulse (see crosshairs). It is seen that a (a) bare pipe, (b) 2-ft. disbond, and (c) 1-ft. disbond are easily distinguishable. The first pulse seen in all three waveforms is noise from the EMATs and electronics. From this figure it is obvious that the disbond size affects both the received signal amplitude and time-of-flight, as predicted by the theoretical and numerical modeling. There is more than a 20- μs difference between the bare pipe case and the 1 ft. disbond case and nearly a 10- μs difference between the 1-ft. and 2-ft. disbond cases. Accounting for the noise level of the system and experimental error, time-of-flight differences in excess of 2 μs can be reliably measured.

As discussed in Section 2, the tendency of attenuation to increase with frequency can be used as a coating disbond detection feature. The absence of coating will result in a frequency spectrum with higher frequency content. As the amount of well-bonded coating increases, higher frequency content will be filtered out by absorption. An experimental demonstration of this concept is shown in Figure 4-7, in which the Short-Time Fourier Transforms (STFTs) of the data sets displayed in Figure 4-5 are plotted. The difference between the two white lines, marking the maximum frequency content of the reference pulse and the first counter clockwise (CCW) traversal, represents the amount of lost frequency content after one complete circumferential traversal of the pipe. The results are summarized in Table 4-2, along with the time and amplitude data, and it is seen that as the disbond size increases, the amount of lost frequency content decreases since there is less coating to absorb it. Therefore, it has been experimentally demonstrated that by monitoring the frequency content of the received signal, it is possible to determine if a coating disbond is present.

Figure 4-8 summarizes the results of the coating disbond proof-of-concept study. All three features are plotted on the same scale. The sensitivity of the technique can be increased by combining the three features into a single feature, such as through addition or multiplication. It should be noted that no discernable reflections were obtained from the boundaries of the disbanded coating regions. It is highly likely that they are very small in amplitude and are absorbed or otherwise lost in the noise floor.

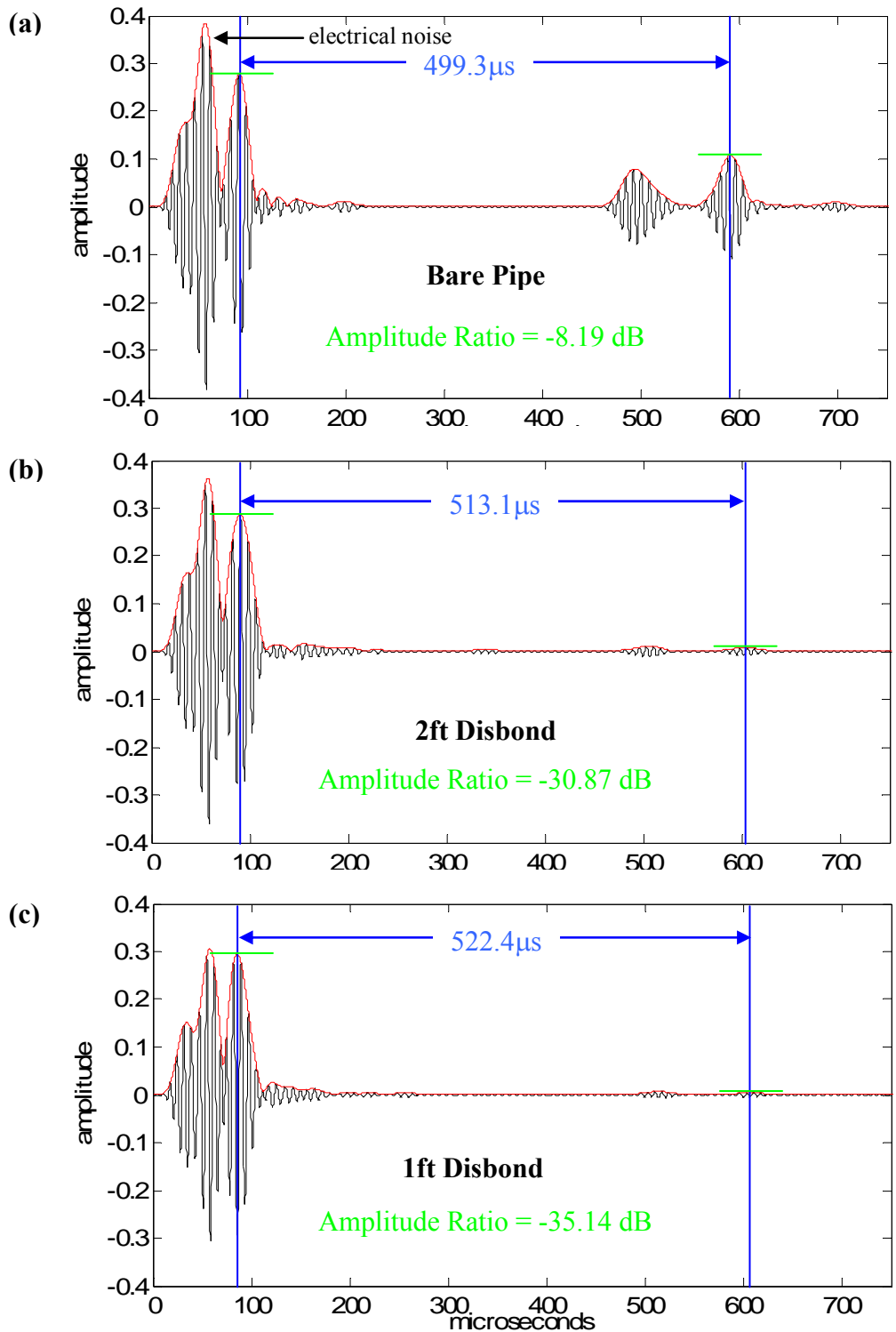


Figure 4-6. Ultrasonic waveforms obtained from a 20-in. diameter schedule 10 pipe with a coal-tar enamel coating with a (a) bare pipe, (b) 2-ft. disbond, and for a (c) 1-ft. disbond.

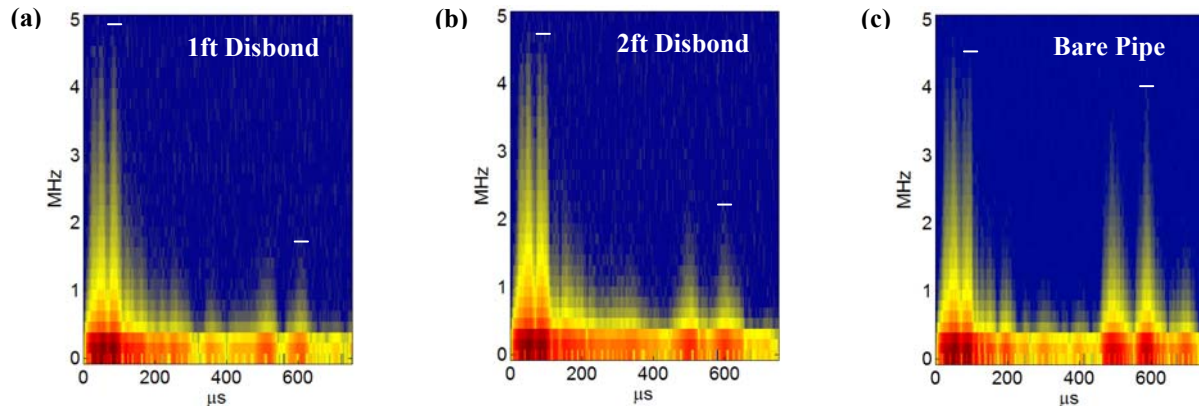


Figure 4-7. STFTs of RF-waveforms for a (a) 1ft disbond, (b) 2ft disbond, and for a (c) bare pipe. Results obtained using a 64-point Hanning window with 32-point overlap.

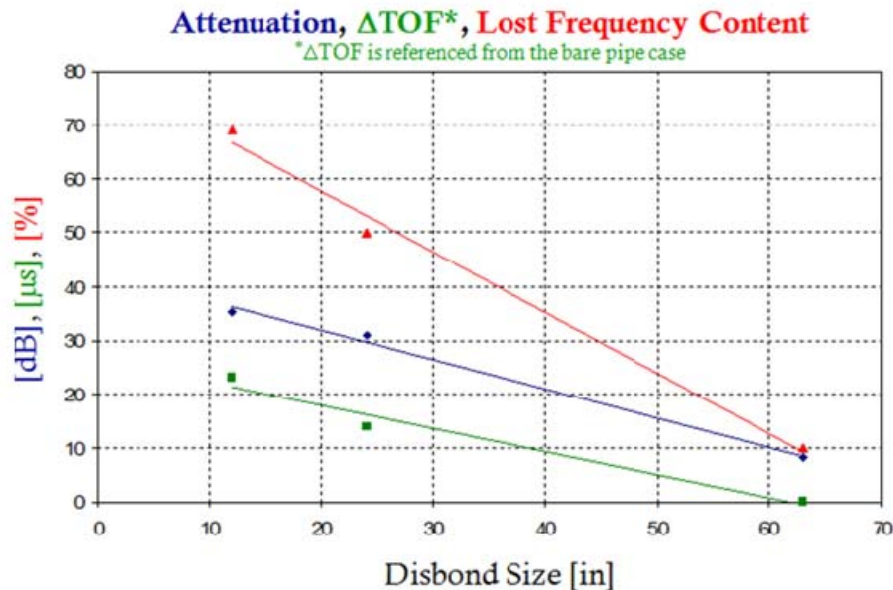


Figure 4-8. A plot showing the time, frequency, and amplitude disbond detection features for three different disbond sizes in a coal-tar enamel coated pipe.

A study wave was also completed to see if the time based coating disbond detection feature could be used with thin coatings. Figure 4-9 shows the SH0 group velocity dispersion curve for a 24-in. pipe with various thicknesses of a coal-tar mastic coating. It is seen that as coating thickness is increased there is a leftward shift in the SH0 mode resulting in lower velocities at lower frequencies. Though not optimized for this coating thickness or type, the 130 kHz EMAT sensor was used to perform a coating thickness experiment. The experimental setup can be seen in Figure 4-10. Transmitting and receiving EMATs were placed on either side of a 2-ft. long coated region of the pipe. The amplitude of the directly transmitted wave packet, indicated by the green arrow, was recorded as the coating layer was made progressively thicker. The envelope of the wave is shown for four different coating thickness stages in Figure 4-11 and the amplitude and time-of-flight results are summarized in Figure 4-12. This experiment demonstrates that it is

possible to perform coating disbond detection on very thin coatings. While time-of-flight changes as small as $0.5 \mu\text{s}$ are difficult to measure in a practical environment, the mode/frequency combination tuned for thin coatings could significantly amplify these shifts. This is a point for future work.

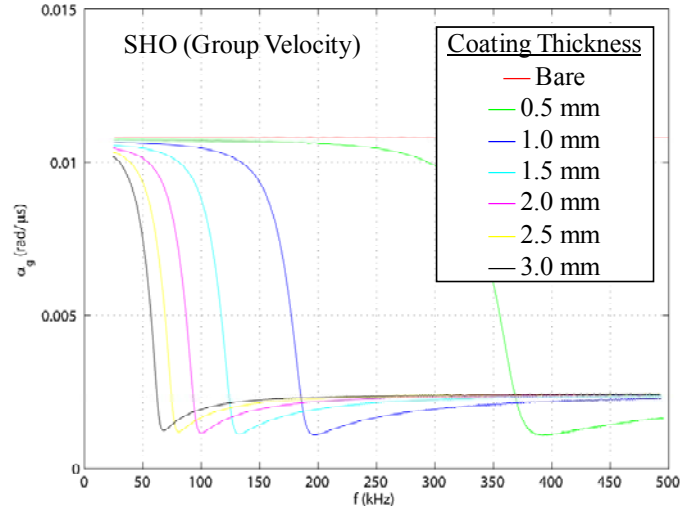


Figure 4-9. Angular group velocity dispersion curve for the SH0 mode in a 24-in. diameter pipe for various coal-tar mastic coating thicknesses.

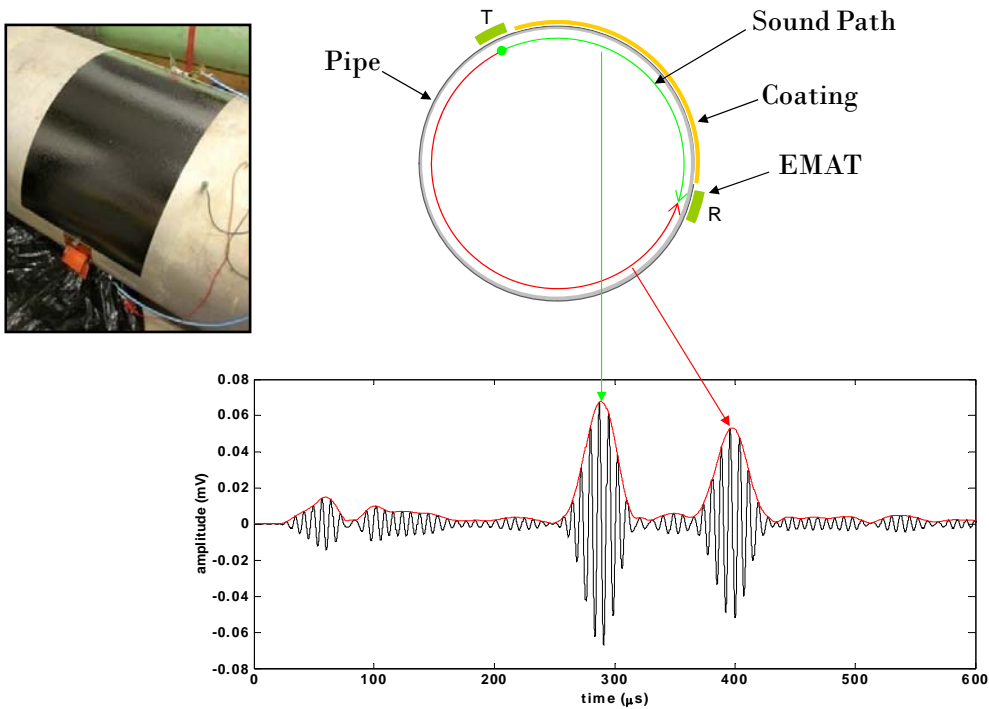


Figure 4-10. Experimental setup used to study the effect of coating thickness on the propagation of a 130 kHz SH-wave. The first packet is the one of primary interest as it has passed directly through the coated region.

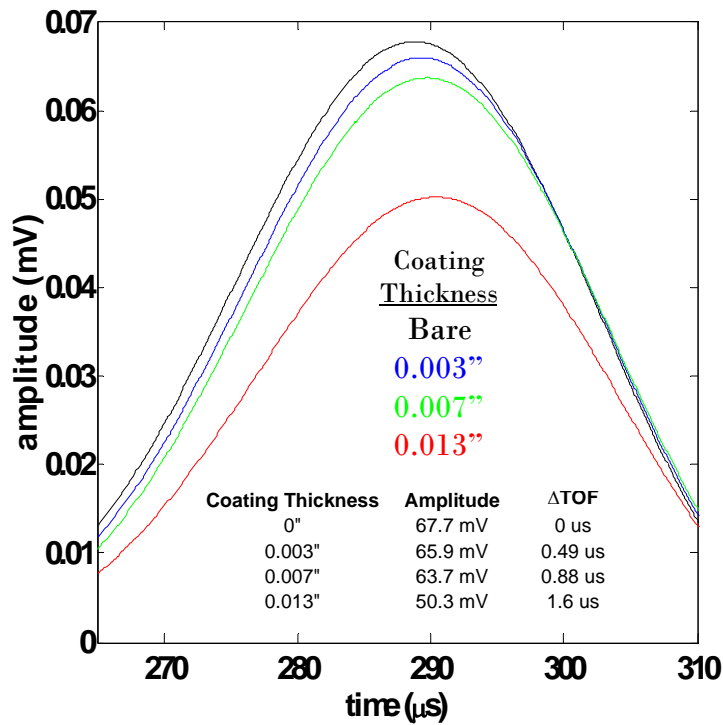


Figure 4-11. Analytic envelopes of the directly transmitted wave packet showing amplitude reduction and time-shifting with increasing coating thickness.

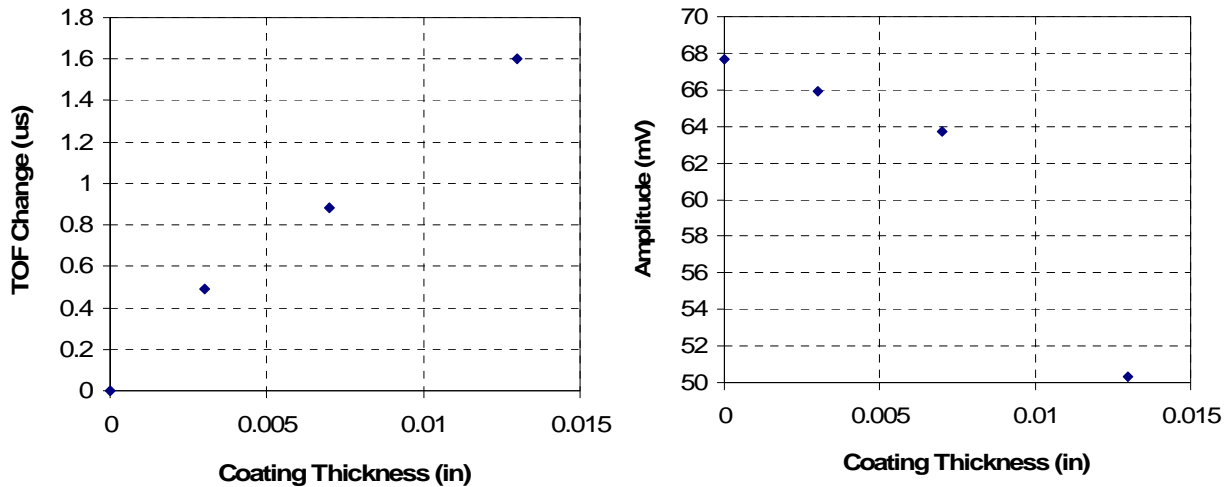


Figure 4-12. Plots showing the time-of-flight and amplitude change as coating thickness is increased.

There are several environmental factors which may potentially affect the detection of coating disbands in buried pipe. These include the following:

- Pressure exerted by soil above the pipe causes the disbonded coating to be pressed against the pipe, though not bonded.

- Where coating disbonds have occurred, the disbonded coating may no longer cover the pipe and compacted soil rests against the bare pipe.
- Water may enter the interface of a disbonded coating.

To test these different scenarios, a 1-sq. ft. disbond was created on a 20-in. diameter pipe with a coal-tar coating. Note, this is the same pipe used to obtain the results shown in Figure 4-8. The disbond area was then covered using two different types of soil, as seen in Figure 4-13. In Figure 4-13(b) the disbond is covered in a clay/sand earth mixture that was obtained from a property where the top soil had been removed. In Figure 4-13(c) the disbond is covered in pottery clay, which was used to simulate the “worst possible case” of soil contamination. Figure 4-14 shows the RF waveforms received in each of the three cases. It is seen that while the soiled interface does produce a noticeable difference in signal amplitude, it does not produce a shift in time. Additionally, the amount of attenuation caused by the clay/sand mixture and pottery clay is significantly less than that produced by a well-bonded coating. The pottery clay attenuated the signal by 2.8 dB and the clay/sand earth mixture attenuated the signal by less than 1 dB. Therefore, it is still possible to detect the coating disbonds when soil is present at the interface. An additional study was completed in which a layer of plastic, to simulate disbonded coating, was placed in between the clay and the pipe surface. Under this condition, there was no change in the RF waveform.

To study the effect of well-compacted soil, a soil box was built at FBS, Inc.’s facility and is seen in the schematic in Figure 4-15 and the photograph in Figure 4-16. The box measures 3 ft. by 3 ft. The box was filled with high clay-content soil and tamped during the filling process to ensure soil compaction comparable to what would be found in the field. Photographs of the soil box, during and after filling, are shown in Figure 4-16. A 6-ft. length of a 20-in. diameter coal-tar wrapped pipe was buried in the box. This particular pipe was previously used for proof-of-concept disbond detection studies. The buried section contained two sections of pipe with removed coating: a 1 ft. by 1 ft. section and a 1 ft. by 2 ft. section. The sections of removed coating can be seen in the middle photograph of Figure 4-16.

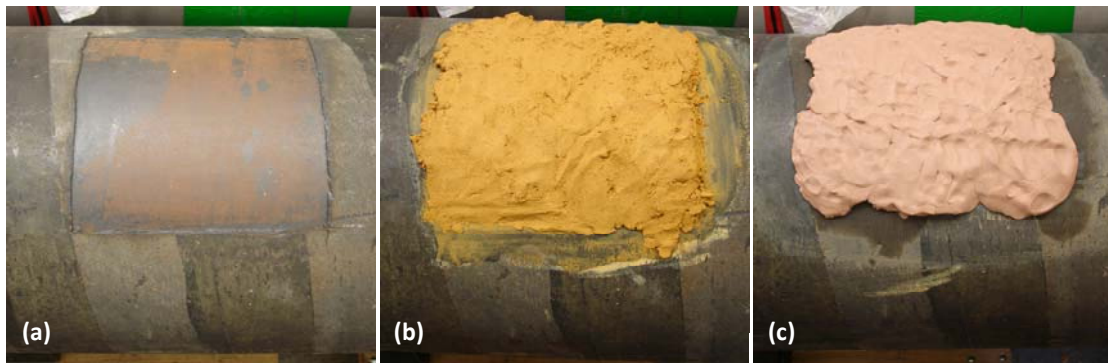


Figure 4-13. Photographs of a 20-in. pipe with a coal-tar coating. (a) disbond with a “clean” interface, (b) disbond with a clay/sand earth mixture present at interface, (c) disbond with pottery clay present at interface. EMATs are on the inside of the pipe on the centerline of the disbond region.

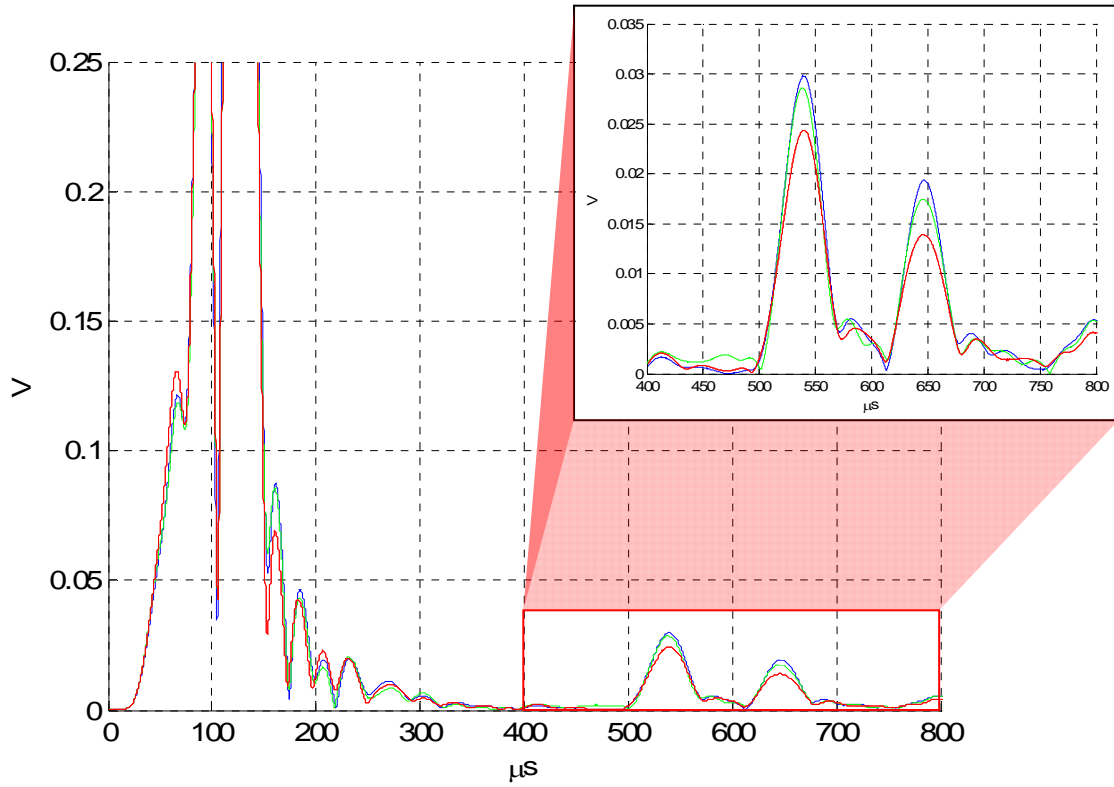


Figure 4-14. RF waveforms showing the signal differences for a “clean” disbond (blue), a disbond with clay/sand earth at the interface (green), and a disbond with pottery clay at the interface (red). A small but measurable difference in amplitude is seen but there is no shift in time.

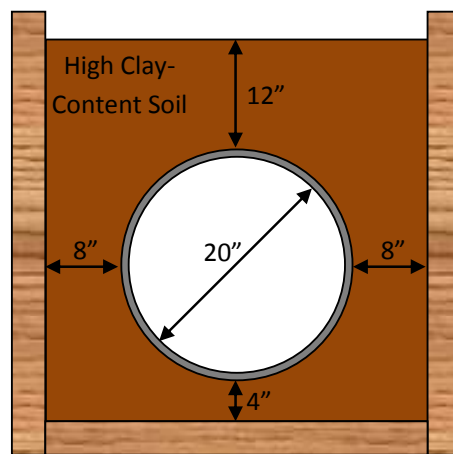


Figure 4-15. Schematic showing cross-section of soil box.

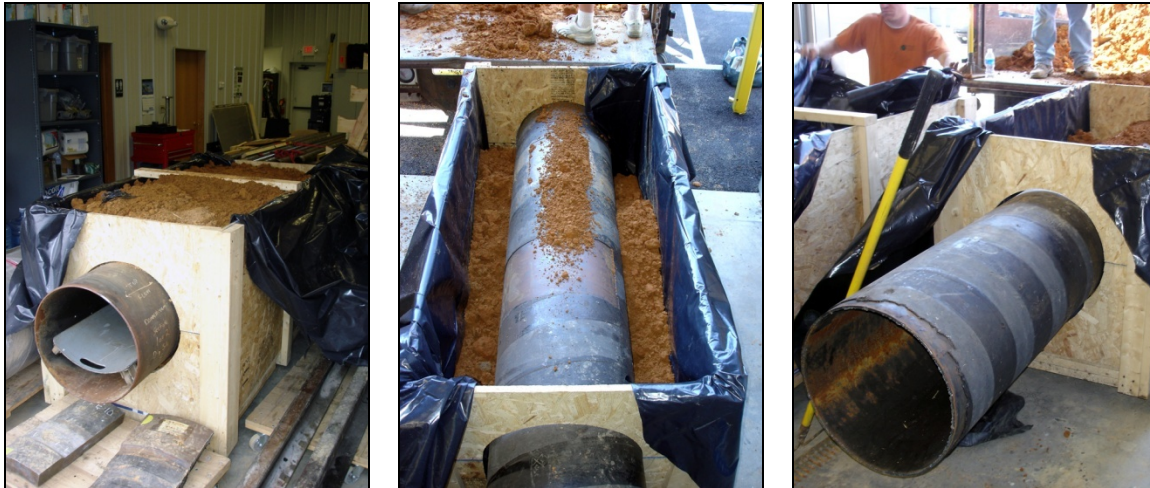


Figure 4-16. Photographs of soil box built for soil loading tests. The 20 in. coal-tar wrapped pipe used in previous studies was buried.

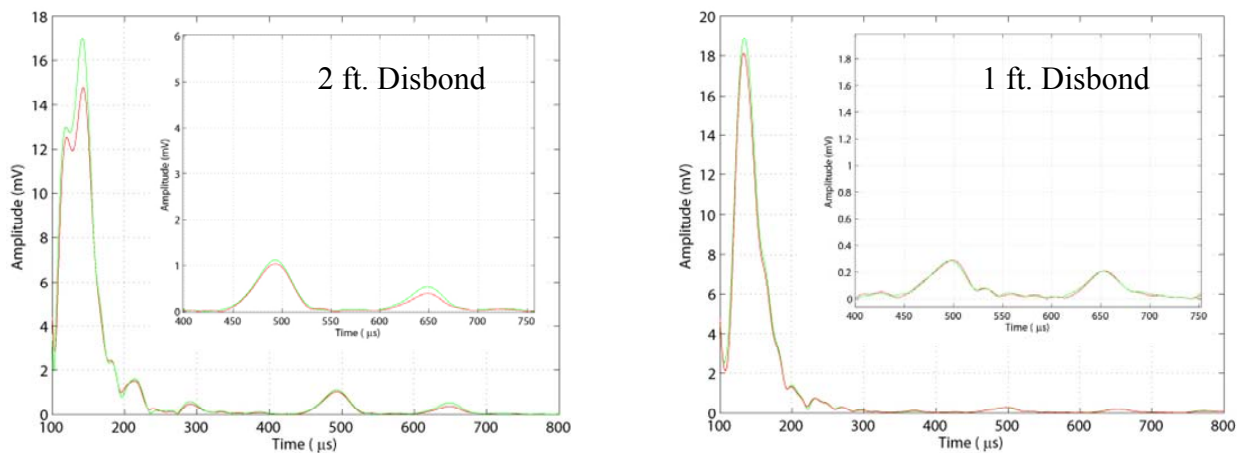


Figure 4-17. Analytic envelopes of RF waveforms obtained from the disbond regions before (green) and after (red) being buried in compacted soil.

The analytic envelopes of the RF waveforms from the regions containing the 2 ft. and 1 ft. disbonds are shown in Figure 4-17, both before (green) and after (red) being buried in compacted soil. It is seen that in the 2-ft. disbond case that there is a loss of several dB in amplitude but no shift in the time-of-flight. For the 1-ft. disbond there is no discernable difference in amplitude or time-of-flight between the two cases. This study is a perfect example of why a multiple-feature disbond detection algorithm is superior to a single-feature detection algorithm.

In summary, the amplitude, time, and frequency-based disbond detection features were verified experimentally. Additionally, it was shown that disbond detection in thin coatings (<1 mm) is feasible. Finally, the influence of soil loading on disbond detection capability was studied and it was found that the soil loading has a minimal effect on signal amplitude and not significant effect on time-of-flight. The effect of the soil is minimal compared to the effect of well-bonded coating.

5.0 Sensor and Hardware Design

5.1. Sensor Design

With interaction from Battelle and BJ Services, FBS, Inc. designed and constructed several prototype EMAT housings that were capable of being integrated with an ILI tool. Several views of the first generation prototype EMAT housing can be seen in Figure 5-1 and Figure 5-2. Several of the key features/components are labeled in the figure. Descriptions of these features/components are as follows:

Housing: The housing serves as the main support and containment structure for the EMAT components. The front and rear sides are beveled to accommodate pipeline protrusions such as girth welds. The front bevel will gradually lift the housing off the surface of the pipe as it crosses a girth weld and the rear bevel will allow for a gradual controlled return. The portion of the housing shown in gray will be machined out of Aluminum 6061-T6 and the portion shown in blue will be machined out of Steel 4140 for wear resistance purposes. The steel wear plate will have several slots machined into the rear portion in order to allow debris to escape from the lip formed by the coil module and the wear plate portion of the housing.

Swing Arm: The aluminum swing arm will serve as the primary mechanical attachment to the main body of the ILI tool. Two pivot points will provide range of motion in the radial direction while allowing the housing to maintain planar contact with the inside surface of the pipe.

Coil Module: The coil module consists of three primary pieces; an Aluminum 6061-T6 reinforcement piece, a mylar/copper EMAT coil, and a 0.015-in. thick titanium wear plate. These components can be seen in Figure 5-2. The mylar/copper EMAT coil is layered in-between the aluminum reinforcement structure and titanium wear plate using a permanent high-strength adhesive. The electrical contact access holes will provide access for wire leads that will run to the body of the ILI tool, where the primary tool electronics will be located. The retention tabs on the reinforcement structure will mate the coil module with the housing wear plate shown in Figure 5-2.

Magnet Pack: The EMAT magnet pack will consist of a total of 98 1 in. \times 1/2 in. \times 1/8 in. Neodymium Boron Oxide magnets, providing an SH-wave wavelength of 1 in. The magnets are arranged in six rows of double-wide alternating-polarity stacks of eight magnets, as seen in Figure 5-3. Each row of the magnet pack is recessed to some depth in such a way that their overall contour will approximately match the curvature of the coil module and internal radius of the pipe. This will provide maximum electromagnetic coupling between the EMAT and pipe wall.

Spring Pad: The spring pads serve as a shock absorbing layer, allowing the coil module to move somewhat independently of the EMAT housing structure. This will help protect the coil module from damage when interacting with pipeline protrusions such as girth welds. The retention tabs seen in Figure 5-2 will rest on top of the spring pads. Alternatively, mechanical springs could be used in place of the spring pads in order to achieve the desired absorption and rebound properties.

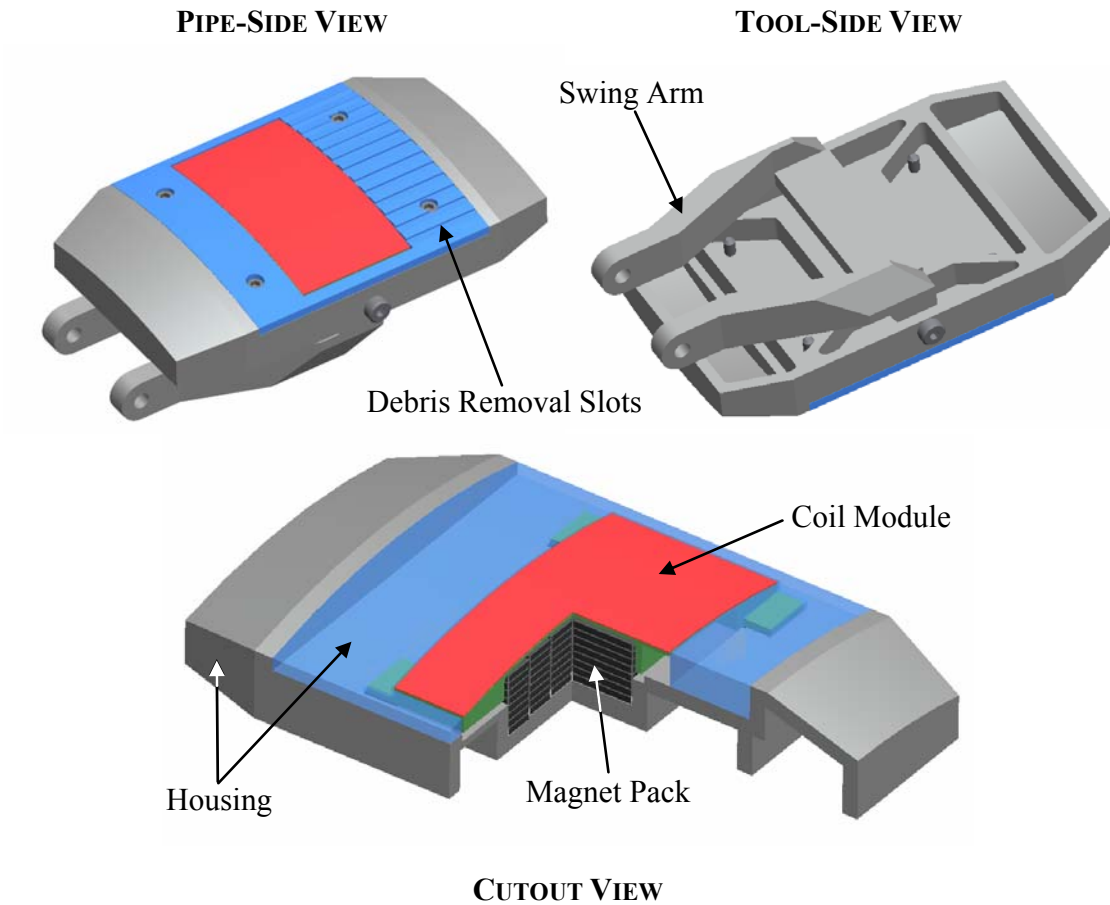


Figure 5-1. Pipe-side, tool-side, and cutout views of the EMAT sensor housing package. One housing package is used for the transmitter and a second for the receiver.

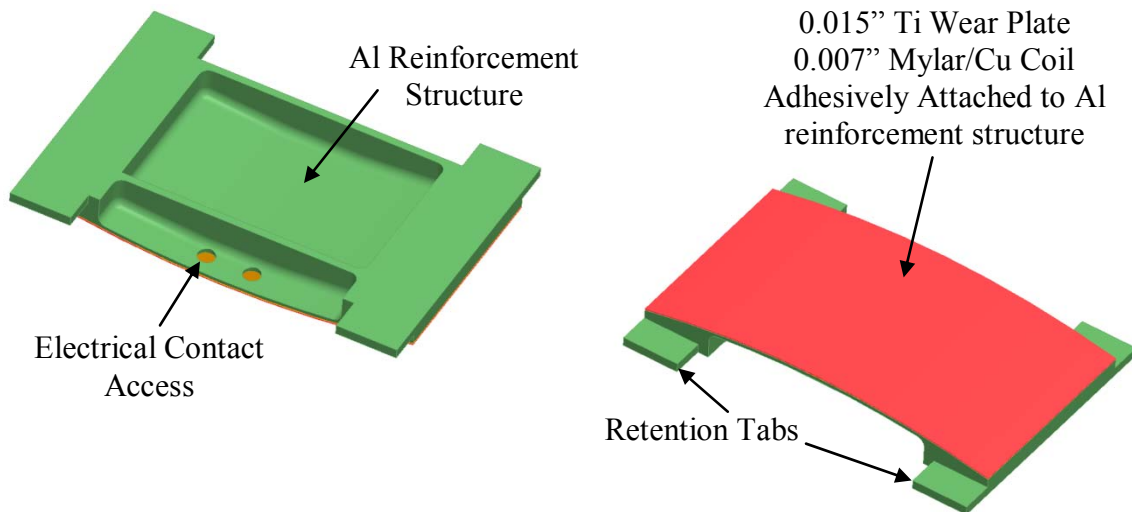


Figure 5-2. Components of the coil module. Titanium wear plate is shown in red and reinforcement structure is shown in green. The EMAT coil can be seen through the electrical contact access holes and is shown in orange.

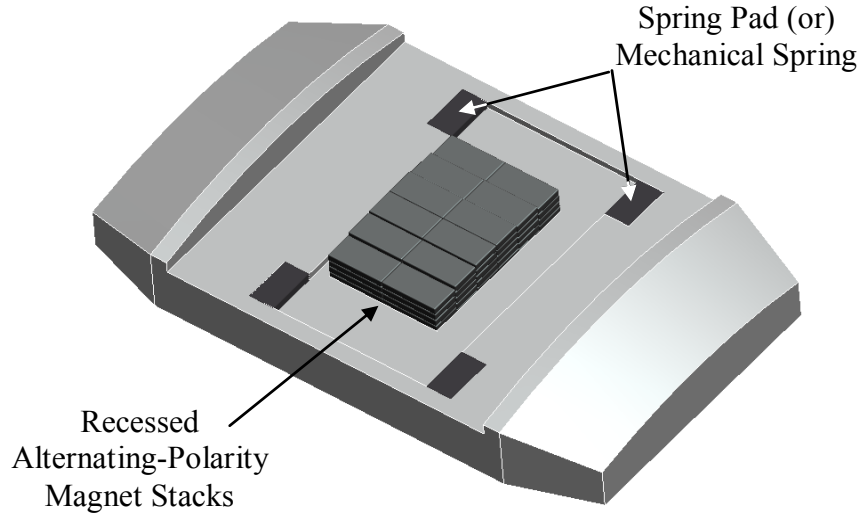


Figure 5-3. Mechanical drawing showing recessed EMAT magnet stack and the spring pads (or mechanical springs).

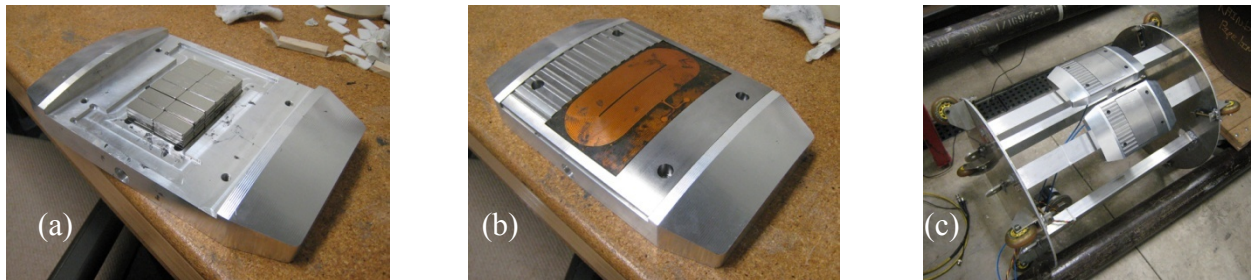


Figure 5-4. Photographs showing the assembled EMAT head where (a) shows the nested magnet package, (b) shows the racetrack coil, and (c) shows the PSF test bed vehicle with the EMATs attached.

Figure 5-4 shows several photographs of the constructed first-generation prototype EMAT heads as well as the test-bed vehicle to which they were mounted for pull-testing. Several minor changes were made to the housing design before the second generation prototype was constructed. A photograph of the second generation EMAT sensor heads and carrier are shown in Figure 5-5. The new carrier design accommodates for the implementation of several sending and receiving sensor pairs. It also allows for adjustable sensor spacing. The new sensor heads consist of the newly designed EMAT coils and a high abrasion resistance polyurethane coating (orange). The second generation sensor heads allow the EMAT coils to sit 0.020 in. to 0.030 in. off the surface of the pipe. With this larger liftoff, it was found that the signal quality was significantly improved by replacing the original steel faceplates with the polyurethane material. The abrasion resistance of the orange polyurethane is approximately 10 times that of ultra-high molecular weight (UHMW) polymers. The first generation sensor head were retrofitted with the new EMAT coils and polyurethane coating. Also seen in the photograph on the right of

Figure 5-5 is the new sensor tuning and pre-amplification network that was designed specifically for the sensors used for this project and will be discussed further in the next section.

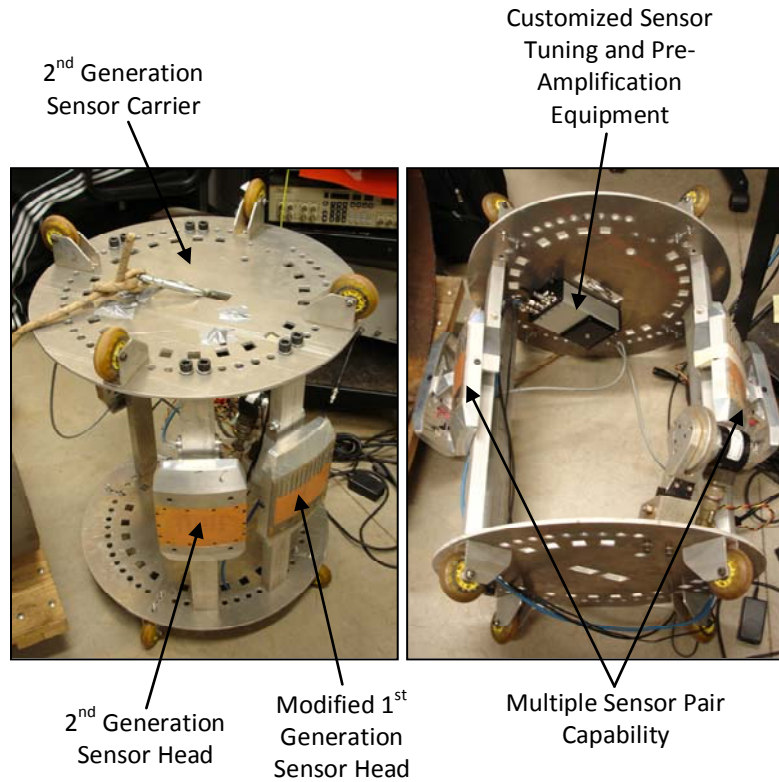


Figure 5-5. Photograph of 2nd generation sensor carrier and EMAT sensor heads. The new carrier has the capability for mounting multiple sensors pairs.

One of the most critical changes to the second generation EMAT heads was the incorporation of a new coil design. Second generation EMAT coils were designed, constructed, and tested with the goal of optimizing penetration power and maximizing sensor liftoff. Table 5-1 includes the specification of all the coils tested. The coils consisted of one printed on mylar film (film), four on Printed Circuit Board (PCB), and one Electrical Discharge Machined (EDM) coil. Unfortunately, the application of an insulation layer to the EDM coil proved to be extremely difficult due to the tight tolerances and it was ultimately decided that efforts were better spent on the development of the other coil types.

Figure 5-6 shows scanned images of the three primary coil geometries. From Table 5-1 it is seen that the primary differences between the PCB coils were the width of the traces and whether or not the PCB had traces printed on both sides (2-layer). The most significant difference between the film coils and the PCB coils is the trace thickness, with the PCB traces nearly 10 times thicker than that of the film coils. By changing the cross-sectional area of the traces the electrical impedance and current density of the coil are changed.

Sensor liftoff experiments were performed with an arbitrary wave generator connected to a 1200V amplifier. It was found that the load applied by the 1200V amplifier was very near the operational limit of the film coils. For this reason, the film coils were not used for pulsing in the 1200V tests. An impedance matching network was used between the amplifier and pulsing coil in all tests.

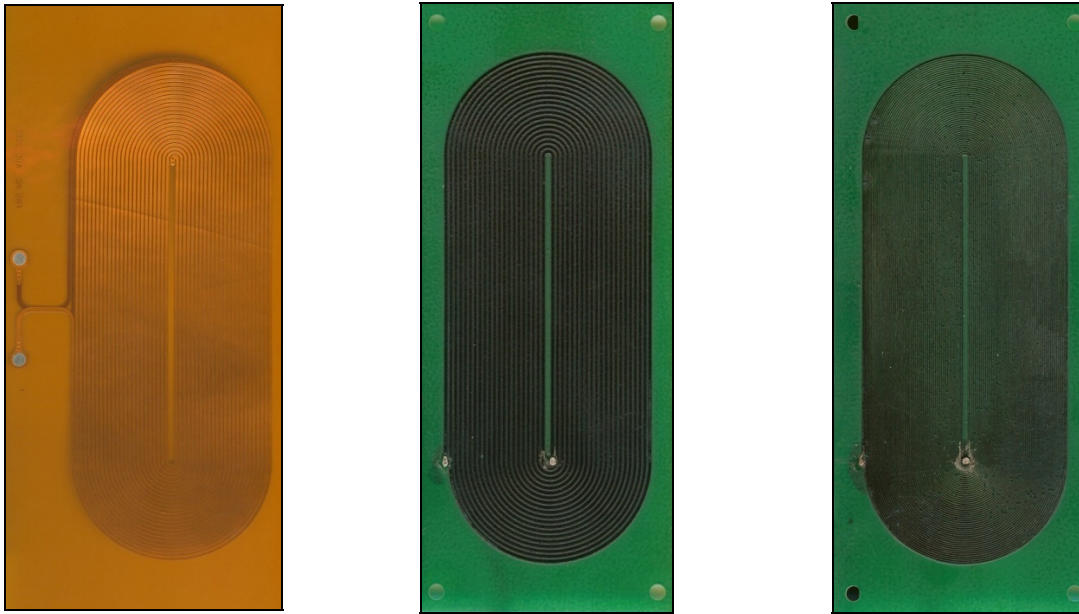


Figure 5-6. Scanned images of mylar film (left), thick-trace PCB (center), and thin-trace PCB (right) coils.

Table 5-1. Specifications of different EMAT coils used in performance evaluation

	No. of Layers	Turns / in.	Trace Width	Trace Thickness	Substrate Thickness
Film	2	~25	~0.03 in	~0.00125 in	~0.005 in
PCB 1	1	~50	~0.01 in	~0.01 in	~0.03 in
PCB 2	1	~21	~0.035 in	~0.01 in	~0.03 in
PCB 3	2	~50	~0.01 in	~0.01 in	~0.015 in
PCB 4	2	~21	~0.035 in	~0.01 in	~0.015 in
EDM	1	~ 21	~0.035 in	~0.05 in	none

Figure 5-7 shows the results of the sensor liftoff study for several of the best combinations of pulsing and receiving coils. It is seen that the single-layer thick-trace PCB coil, used as a pulser, and the mylar film coil, used as a receiver, are the optimal sensor pair. For nearly all liftoff distances, this combination of coils provided the highest amplitude. Also of interest is the PCB2/PCB3 coil combination. This is because these two coils are very similar in construction

and are, in general, slightly more robust than the film coils. From an implementation standpoint, a more robust coil may be preferred over several decibels of signal amplitude.

Shown in Figure 5-8 is a comparison of the PCB2/Film coil combination for both the 1000V and 1200V systems. By switching from the 1000V system to the 1200V system, there is a gain of nearly 8dB in signal amplitude. This proves that moving from a 1000V system to a 1200V system is incredibly advantageous despite the need for a more “heavy-duty” pulsing coil. Also shown in Figure 5-7 is a comparison of the original coil combination (Film/Film), used in all previously reported tests, and the new optimal coil combination (PCB2/Film). There is, approximately, an 11dB gain in signal amplitude by switching to the new pulsing coil design. Ultimately, it was decided to use the PCB2/PCB3 coil combination as it was the more robust option.

This page intentionally blank.

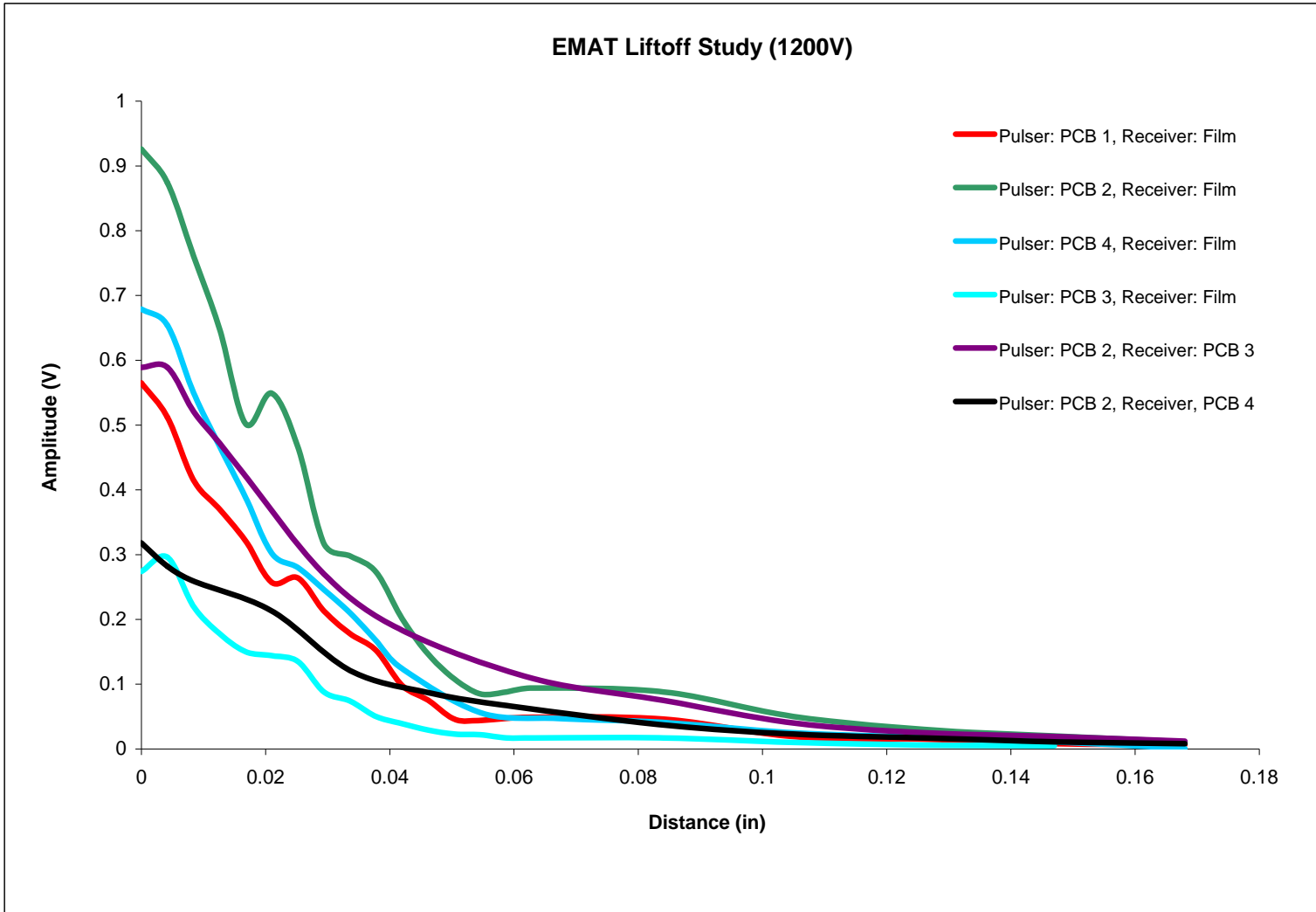


Figure 5-7. Plot showing the received signal amplitude vs. sensor liftoff for the best pulser/receiver combinations.

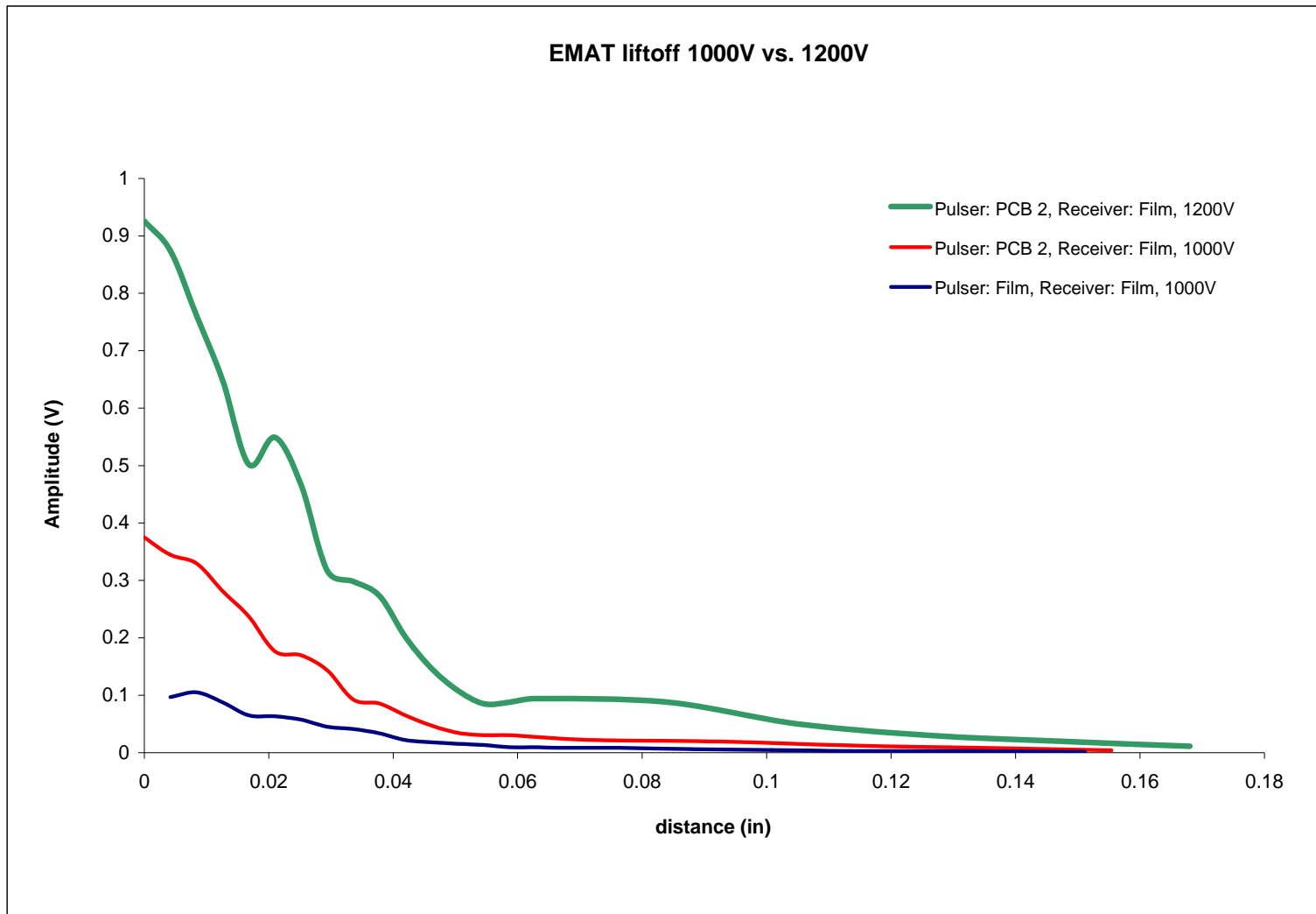


Figure 5-8. Plot showing the received signal amplitude vs. sensor liftoff for the optimal coil combination for both 1000V and 1200V systems.

5.2. Hardware and Software Design

Figure 5-9 shows a flow diagram between the key system components. The 10 counts/in from the encoder are sent to the digital counter where they are up- or down-sampled to produce a trigger in the increments specified by the user in the software waveform setup controls. A trigger is then passed to the A/D card and the receiving channel is activated and the trigger is relayed to the arbitrary waveform generator (ARB). The ARB outputs +/- 1V rectangularly windowed 130kHz sine wave into the 1200V amplifier. The amplifier turns sine wave to 1200V square wave. The pulse then travels through the matching network, which matches the impedance of the transmitting coil. From the matching network the pulse travels to the transmitting EMAT which generates a guided wave in the wall of the pipe. The guided wave travels through the pipe wall to the receiving EMAT. Because the received voltages are typically very low, the received pulse is sent through a pre-amplifier before it is passed to the A/D to be digitized, processed, and displayed on screen or sent to a storage device. The details of some of the key electronic components are summarized in Tables 5-2 through 5-5.

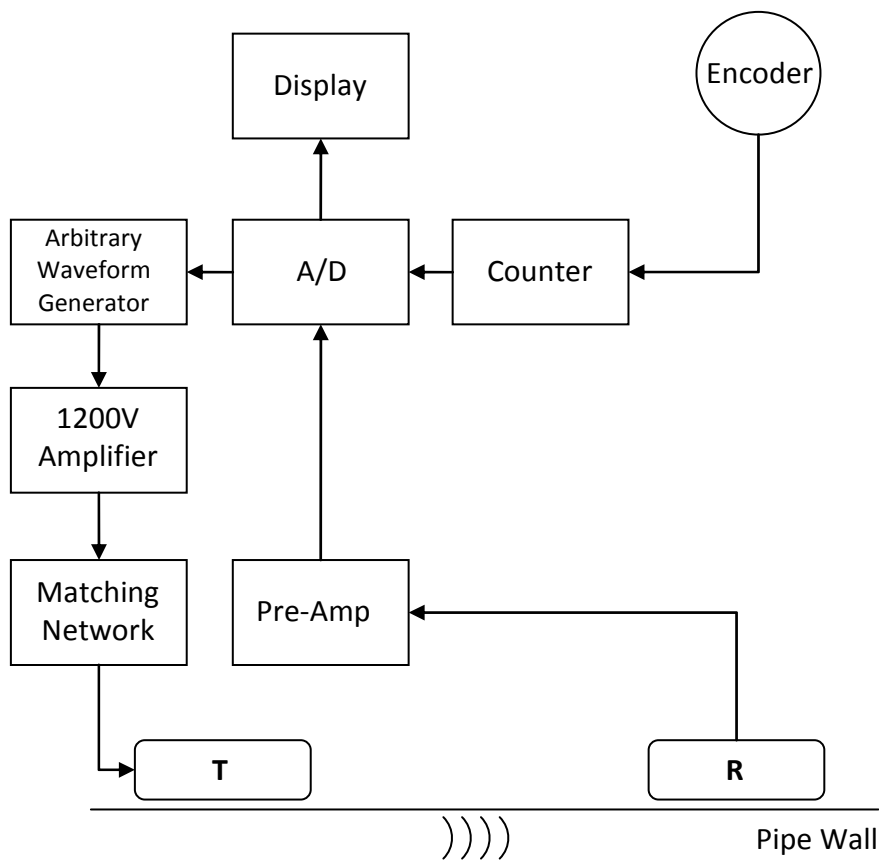


Figure 5-9. System flow chart showing key components.

Arbitrary Waveform Generator



Table 5-2. Specifications of arbitrary waveform generator.

Analog output channels	1
Amplitude Range	10mV to 10V full scale (50 ohms)
Resolution	14 bit
Output Current	200mA peak
Sample clock	100 MSample/sec
Output bandwidth	100Hz to 15MHz
Memory	512 KSamples max
Operating Modes	Free run, programmable single shot, programmable repetitive, external trigger
Form factor	PCI full slot

Analog-to-Digital Converter



Table 5-3. Specifications of A/D card.

Resolution	8 bit
Bandwidth	100 MHz max, 20 MHz typical
Sample clock	100 MHz
Channels	2 Simultaneously sampled
Memory	16 MB
Vertical range	+/- 25mV to +/- 25V
Trigger	External edge
Trigger range	+/- 10V

Digital Counter



Table 5-4. Specifications of digital counter.

Counters	2
Resolution	32 bit
Sample clock	80 Mhz
Output	+/- 5V

1200V Toneburst Amplifier



Table 5-5. Specifications of 1200V amplifier.

Mode	Square wave
Output	+/- 600 V
Frequency Range	20-200 kHz

Figure 5-10 shows two screenshots from the waveform processing and display software developed by FBS, Inc. for displaying ILI data. The “Waveform” screen (top) contains all waveform filtering options and the “Averaging” screen (bottom) contains options for spatial signal averaging. Spatial averaging is employed because the sensor is never in one location long enough to perform temporal averaging. In the spatial averaging algorithm, the waveform obtained at the indicated position is averaged with the waveforms to the right and left of the indicated position. The user can input the number of waveforms to be averaged. Typical averaging numbers include 3, 5, or 7 waveforms.

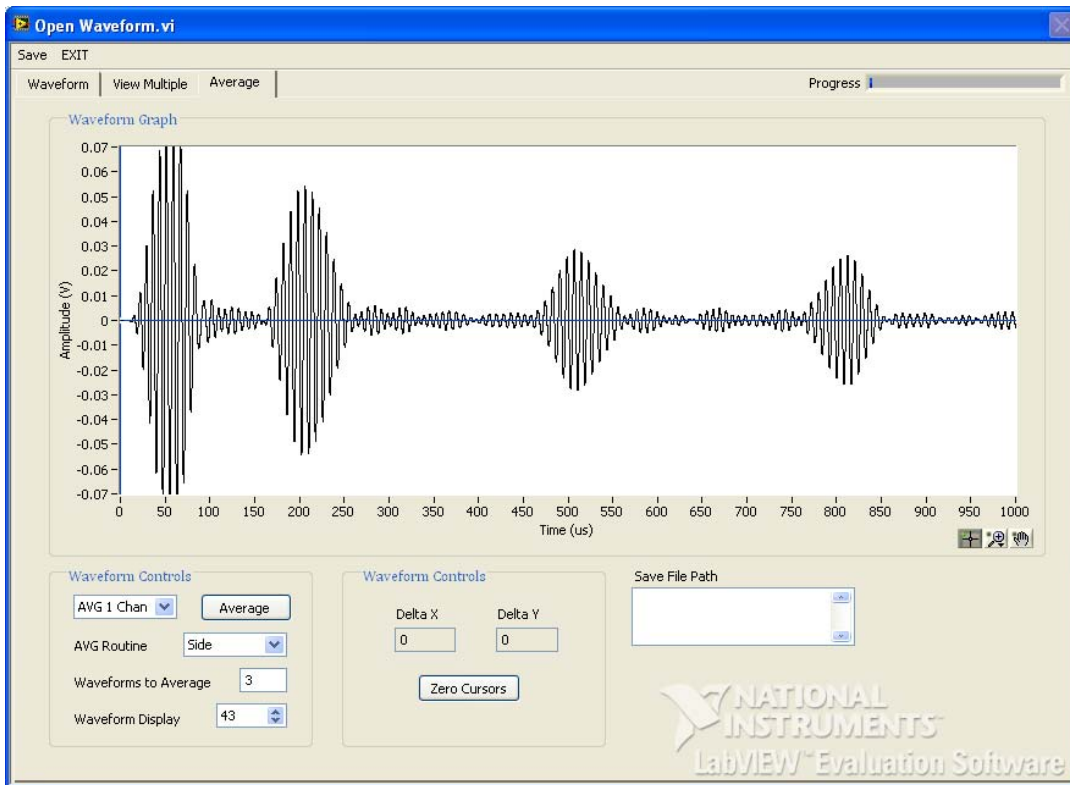
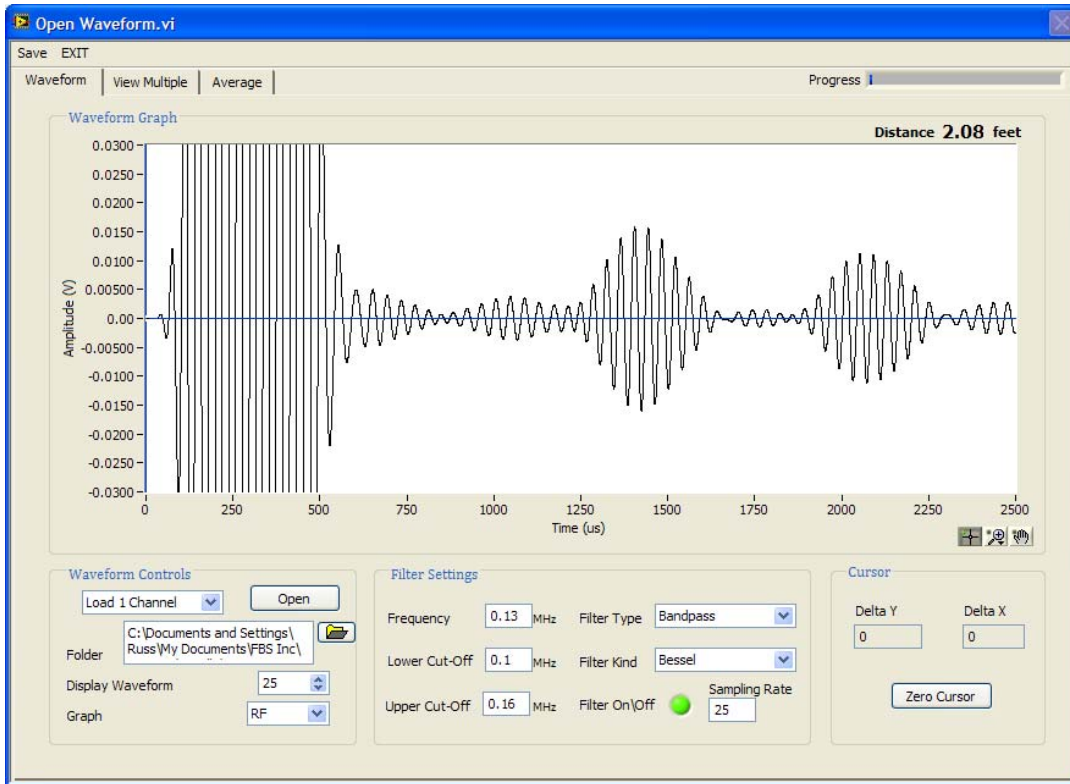


Figure 5-10. Screenshots of waveform display software developed for processing and viewing ILI data. Top screen contains filtering settings and bottom screen shows spatial averaging options.

6.0 Results of Pull Tests

This sections contains the results of three separate rounds of pull tests, two of which were completed at Battelle’s PSF in West Jefferson, OH and one of which was completed at BJ Services’ facility in Calgary, AB, CA. Following the presentation of the results, some general observations about the pull tests and the performance of the tool are made.

6.1. Round 1: Battelle PSF, West Jefferson, OH

Four pipes were prepared for pull testing at Battelle’s PSF. All pipes were 24 in. in diameter. Three of the pipes had coating applied to the outer surface of the pipe. A photograph of the four samples can be seen in Figure 6.1 and a description of each pipe can be found in Table 6-1. The internal surfaces of all four pipes had been sandblasted and coated with primer to prevent corrosion.



Figure 6-1. Photograph showing four pipes used for pull testing at the PSF.

Table 6-1. Description of pipe samples used for pull tests at the PSF.

Name	Description	Size (OD, Length, Thickness)
Pipe 1	Bare pipe, free of defects.	24" × 270.75" × 0.300"
Pipe 2	Coated in a fibrous coal-tar wrap with several large disbonded sections, dents, and several simulated and real cracks.	24" × 274" × 0.270"
Pipe 3	Tape wrap with one disbonded section, no defects noted.	24" × 254" × 0.310"
Pipe 4	Fusion-Bonded Epoxy coating with several disbonded regions and simulated defects.	24" × 203.5" × 0.362"

The test-bed vehicle was pulled through the pipes using a tow winch with a variable speed controller. Pull speeds ranged from 0.3 mph to approximately 1 mph. The speed controller would not allow for pull speeds greater than this. Another limitation on pull speed was due to the incrementation setting of the encoder. If pulled too quickly, the triggering from the encoder would cause the pulser to exceed its duty cycle. This issue was remedied before the second round of pull tests with the incorporation of a software conditioner for the encoder.

Runs were completed on each of the four pipes. Figures 6-2 through 6-5 show three-dimensional plots of the data sets obtained from each run. To generate these plots, the analytic envelope of the RF signal is plotted versus the axial location at which it was obtained. The result serves as a quick reference for the evaluation of each data set. Figure 6-2 shows the result obtained for Pipe 1, which was bare. It is seen that both the CW and CCW traversals are both present and relatively uniform in nature.

Figure 6-3 shows the results obtained from Pipe 2, coated with a fibrous coal-tar wrap. Several disbond regions as well as other features can be seen in this figure. Figures 6-6 and 6-7 show the disbond detection feature analysis for a section of bare pipe and for a section with an approximate 50 percent disbond. Table 6-2 summarizes these results along with the results for several other axial locations containing disbands. It is seen from these figures that, though the amplitude is low, the traversal that travels around the full circumference is successfully able to detect all 24 in. disbands using the amplitude-, time-, and frequency-based detection features. An 8 in. disbond present in between 53 in. and 92 in. was not detected because the signal was completely attenuated by the coating that was well bonded. This is an indication that an actual implementation will need at least two sets of sensor heads.

Figure 6-4 shows the data acquired on Pipe 3, which had a wrapped coating. Due to the highly attenuative nature of this coating, the disbond was not detected as the wave was completely absorbed by the well-bonded coating. Again, this can be avoided in the future through the incorporation of additional sensors. The point at which the sensors enter the coated region can be seen in Figure 6-4.

Figure 6-5 shows the data set collected on Pipe 4 with the fusion-bonded epoxy coating. While the traversal signals are clearly seen, disbond detection information could not be extracted from the signals due to the mild nature of the coating. Any variations in the disbond detection variables were not large enough to exceed the variation caused by random noise. Though it was proven to work in the laboratory it is recommended that for the practical detection of disbond in FBE-like coatings, a different (higher frequency) sensor design should be employed.

Pipe 1 (No Coating)

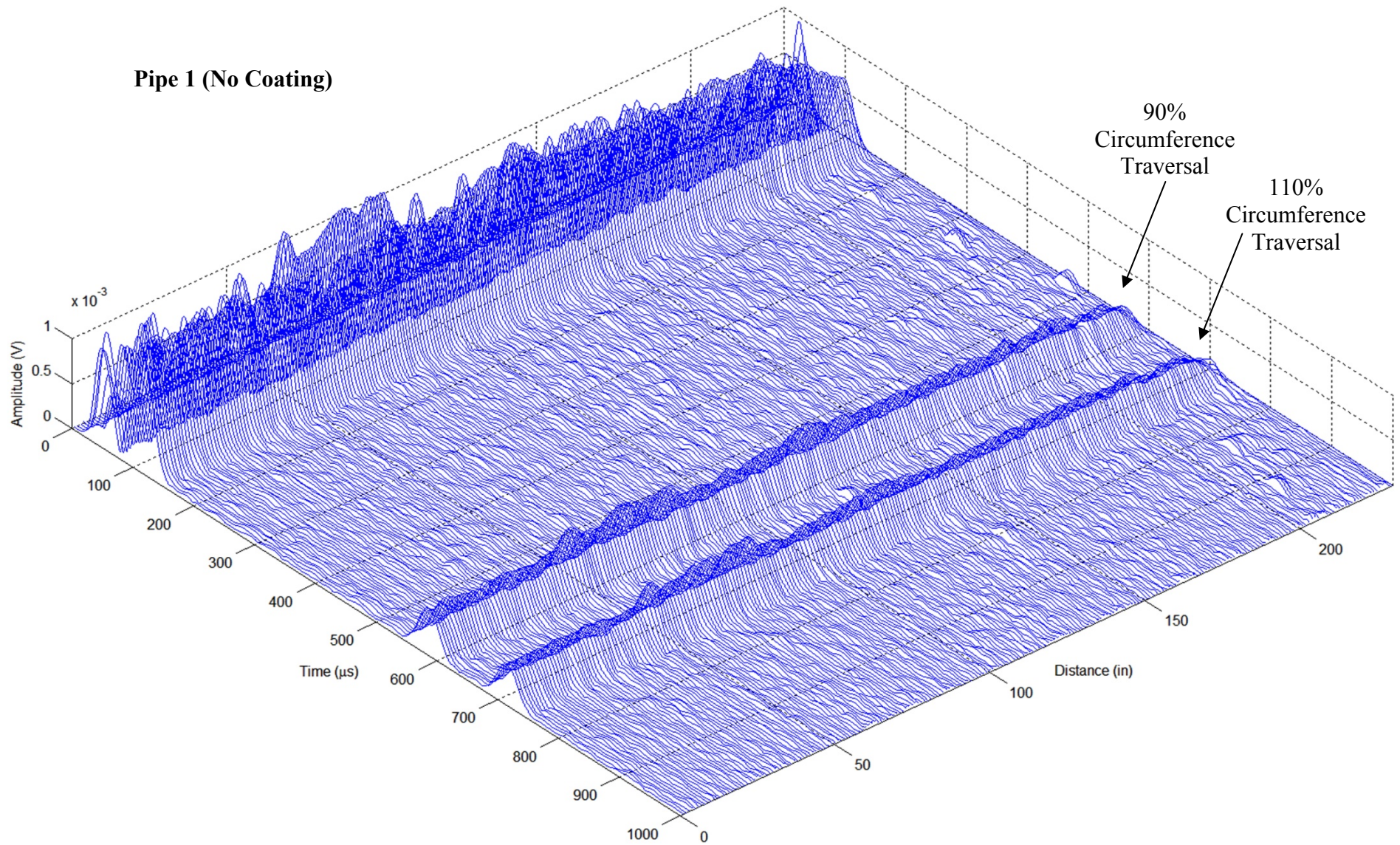


Figure 6-2. Three-dimensional plot of analytic envelopes of ultrasonic data acquired on Pipe 1, which is bare.

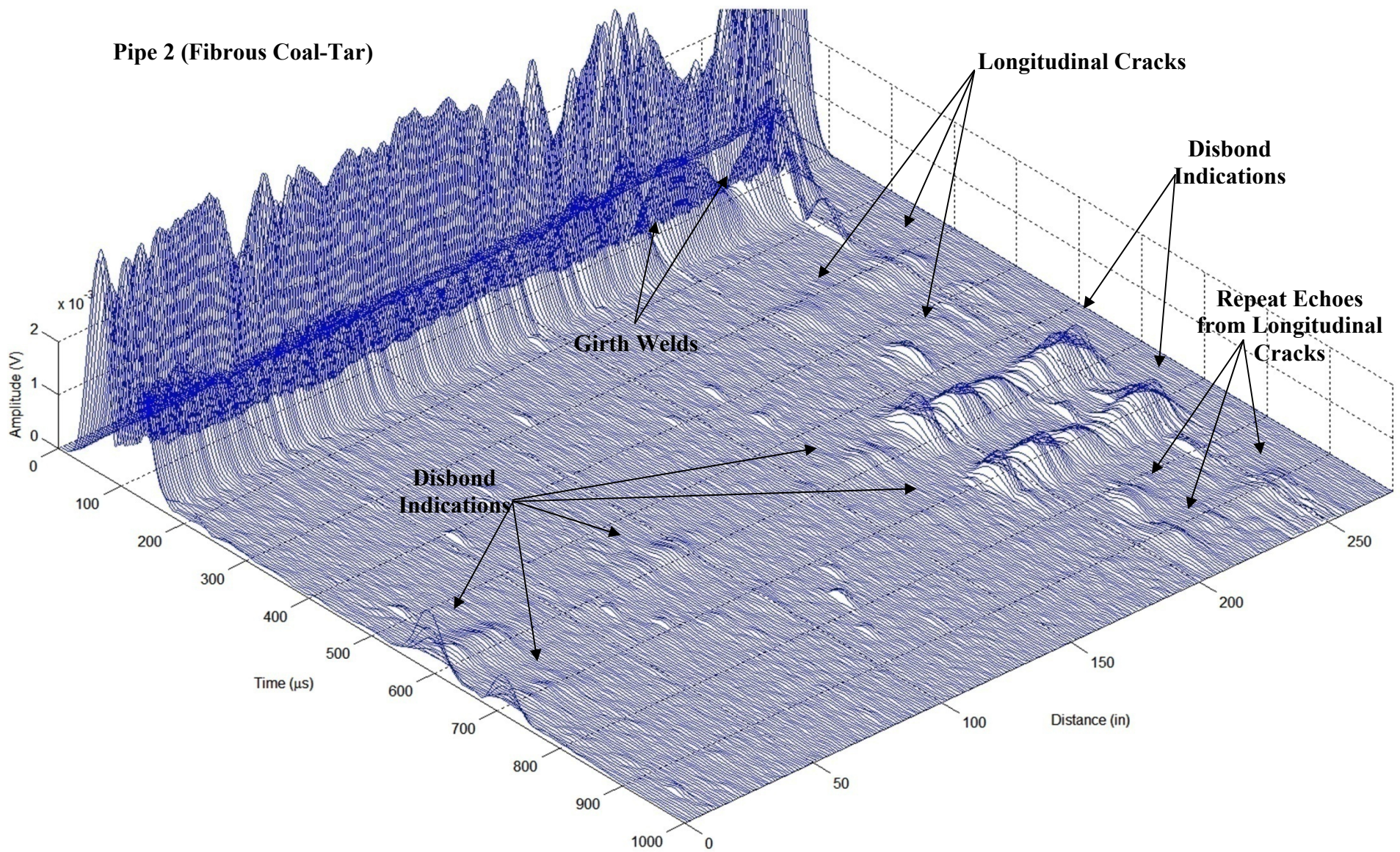


Figure 6-3. Three-dimensional plot of analytic envelopes of ultrasonic data acquired on Pipe 2, which is coated with a fibrous coal-tar coating.

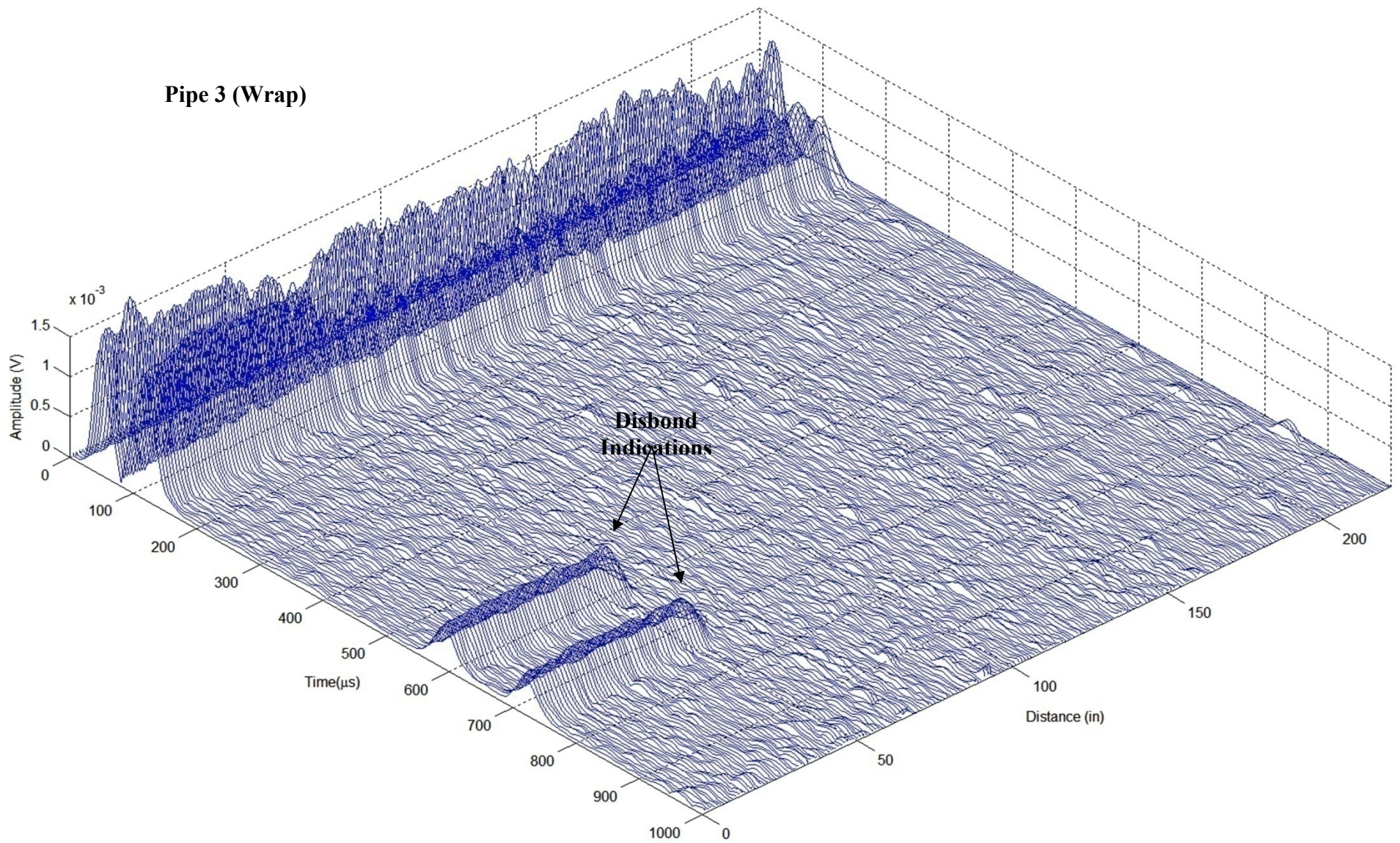


Figure 6-4. Three-dimensional plot of analytic envelopes of ultrasonic data acquired on Pipe 3, which is coated with a wrap coating.

Pipe 4 (FBE)

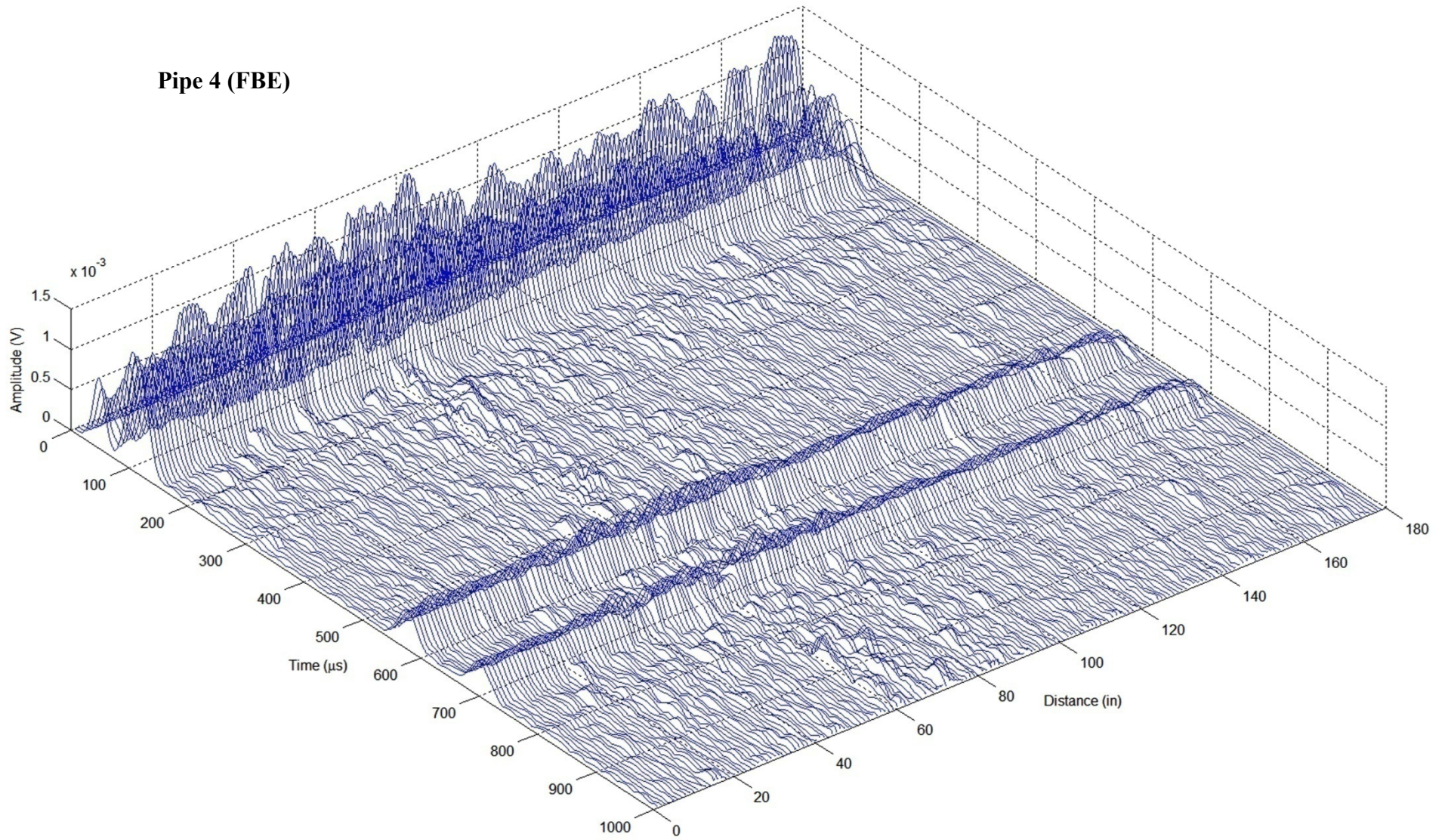


Figure 6-5. Three-dimensional plot of analytic envelopes of ultrasonic data acquired on Pipe 4, which had an FBE coating. The decreased signal-to-noise ratio seen in this plot was caused by a grounding issue with one of the EMAT sensors.

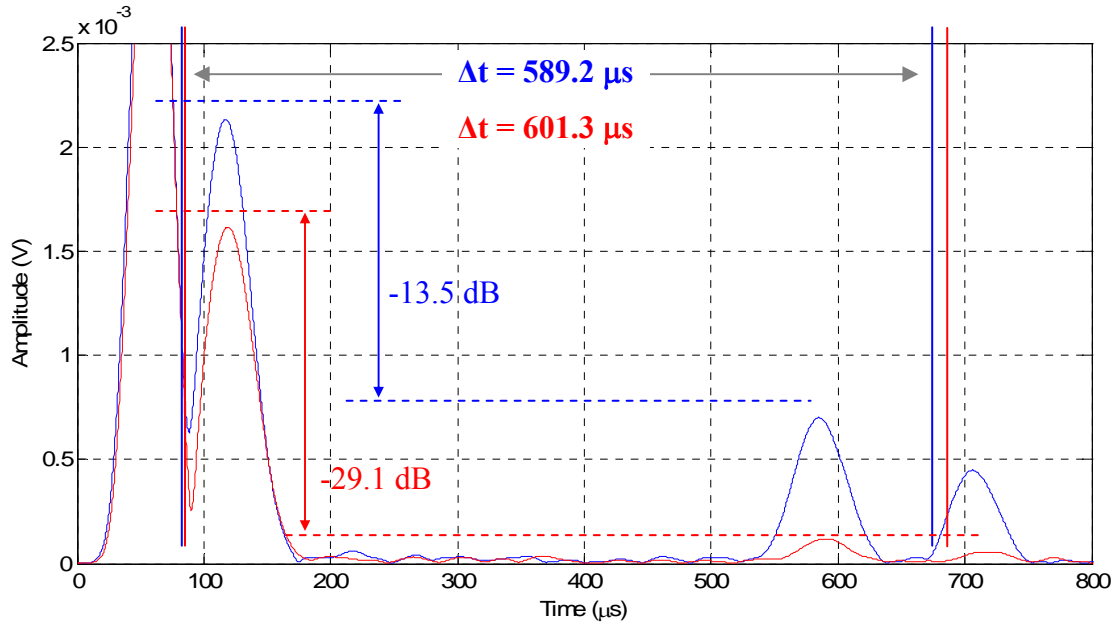


Figure 6-6. Two-dimensional plot of analytic envelopes of ultrasonic data acquired on Pipe 2 at 1 in. into the pull length (blue) where the pipe was bare and 27 in. into the pull length (red) where an approximate 50-percent circumference disbond existed.

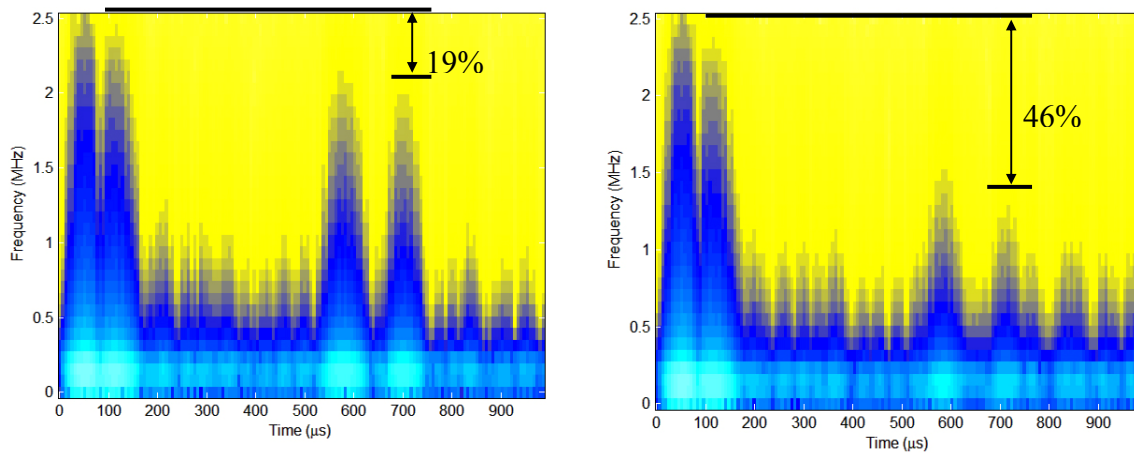


Figure 6-7. Short-Time Fourier Transform of ultrasonic data acquired on Pipe 2 at 1 in. into the pull length (left) where the pipe was bare and 27 in. into the pull length (right) where an approximate 50-percent circumference disbond existed. A 64-point Hanning window with 32-point overlap was used to obtain these plots.

Table 6-2. Summary of disbond detection results for several pull locations for Pipe 2 (Fibrous Coal-Tar Coating).

Pull Location	Disbond Size	Amplitude Loss	Time-of-Flight	Lost Frequency Content
1 in.	100%	-13.5 dB	589.2 μ s	19%
27 in.	~ 30%	-29.1 dB	601.3 μ s	46%
99 in.	~ 30%	- 25.9 dB	596.5 μ s	41%
170 in.	~ 30%	-27.8 dB	599.9 μ s	46%

6.2. Round 2: Battelle PSF, West Jefferson, OH

Though originally not planned, a second round of pull tests at Battelle’s PSF were added to the project scope in order to test the second generation sensor heads and carriage prior to the pull-tests at BJ Service’s facility in Calgary. The focus of this round of tests was not to demonstrate disbond detection capability but to test the capabilities of the new sensors. For this reason pull tests were only performed on the bare pipe and the coal-tar enamel coated pipe described in Section 6.1.

Figures 6-8 and 6-9 show some sample data acquired on the coal-tar enamel coated pipe during the second round of pull tests at the PSF facility, completed in November 2008. Figure 6-8 shows the analytic envelope of a signal acquired in a section of the pipe where the coating had been completely removed. The first large pulse seen is from electromagnetic noise and the second two pulses, marked with blue and red cursors, are the received ultrasonic signals. The pulse marked with the blue cursors would be used as a reference pulse and the pulse marked with red cursors is the wave that has traveled around approximately 2/3 of the pipe circumference. The pulse that completely traverses the circumference is attenuated by the coating, indicating that multiple sensor pairs will probably be needed for full circumferential inspection. Figure 6-9 shows the data acquired in a section of coated pipe with a disbond. It is seen that there is about a 14 μ s difference in time-of-flight as compared to the bare pipe, as well as a significant decrease in amplitude.

Figure 6-10 shows that RF waveform obtained during a pull through the bare pipe specimen at a tool speed of approximately 4 mph. The waveform is displayed in the data processing and viewing software developed for this project. Spatial averaging is employed in place of time averaging to improve the signal-to-noise ratio.

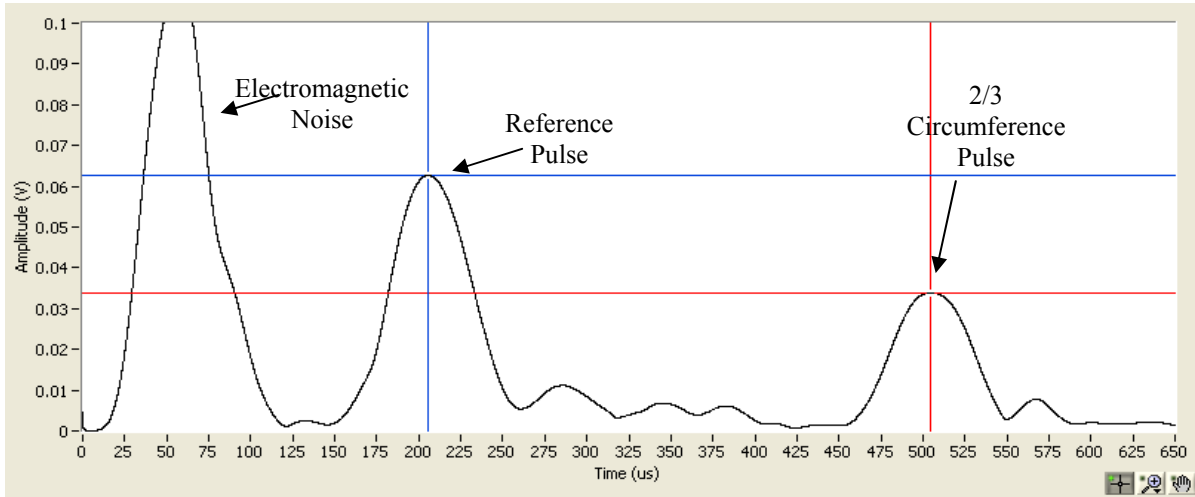


Figure 6-8. Analytic envelope of the ultrasonic signal obtained in a bare section of pipe.

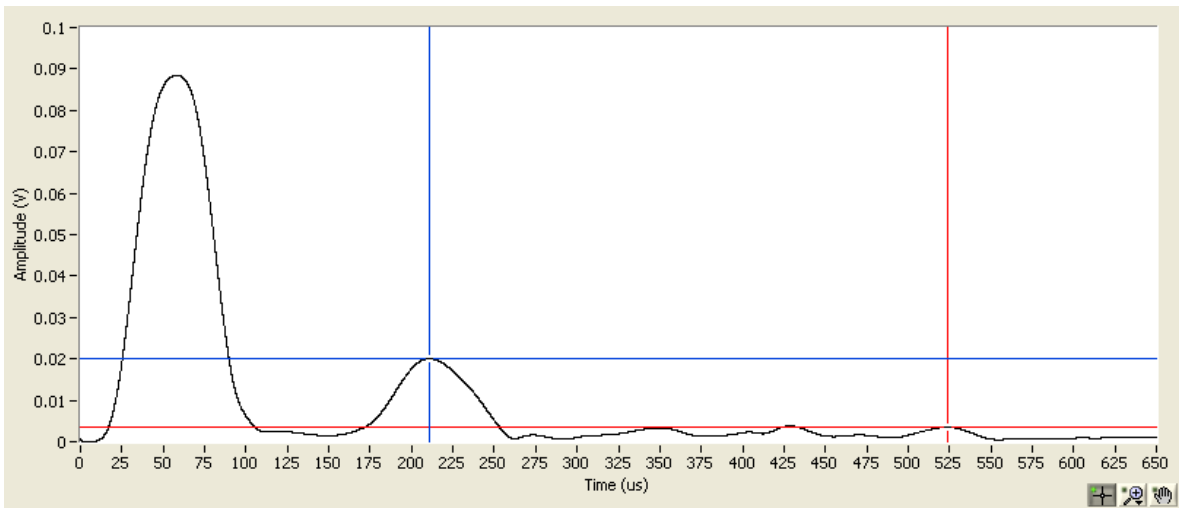


Figure 6-9. Analytic envelope of the ultrasonic signal obtained in a section of pipe with a disbond in the coal-tar enamel coating.

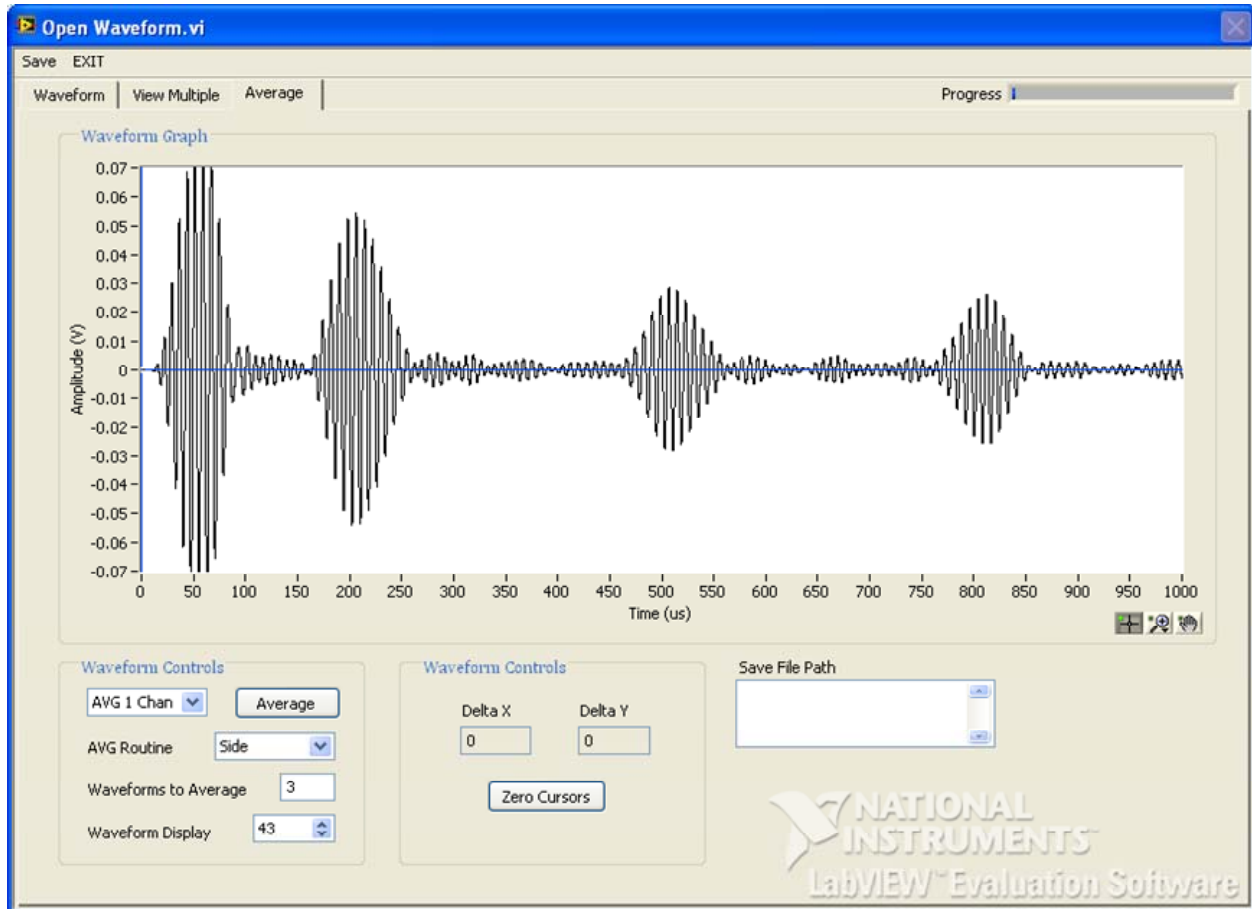


Figure 6-10. RF waveform obtained during a pull through a bare pipe at a speed of approximately 4mph. As seen in the screenshot of the FBS, Inc. developed software, spatial averaging is employed to improve the signal-to-noise ratio.

6.3. Round 3: BJ Services, Calgary, AB, CA

After the second round of pull tests, a new EMAT tuning card was acquired which optimized the tool for dual transmitters and receivers, allowing full circumferential inspection using two sensor pairs. Unfortunately, during shipment from the U.S. to Canada the arbitrary waveform generator was damaged and could not be used for the third round of pull tests. A back-up card was brought along but was not optimized for the application, essentially limiting the maximum pull speed to several mph and with a much lower signal-to-noise ratio. Nonetheless, some pull data was still acquired.

Several 24-in. diameter specimens with coal-tar enamel coating, totaling several hundred feet, were assembled on BJ Services' pull-rig. Due to some misaligned and dented joints, it was decided that the electronics would not be pulled through the entire rig as they were not ruggedized. Instead they would be pulled through just one section not containing any joints. The sensors and carriage were, however, pulled through the entire rig to test their survivability. Again, the focus of this round of pull test was not so much to prove disbond detection capability as it was to demonstrate the survivability of the sensors.

Figure 6-11 shows a photograph of the pull rig setup at BJ Services' facility. Figure 6-12 shows a photograph of the prototype ILI tool with the sensor carriage in the pipe and the electronics carriage sitting in the staging area. All required electronics fit within the electronics carriage and can be run off battery power if necessary. A 1500VA uninterruptable power supply was capable of running all required electronics for more than 1.5 hours. Much longer run times could be achieved with the more advanced batteries that are typically used in MFL ILI tools.

Figure 6-13 shows sample results from a hand-pull through a bare pipe section at BJ Service's facility. Two channels are used to obtain a full circumference inspection. There is a noticeable drop in signal amplitude compared to the result shown in Figure 6-10 obtained in a bare pipe section during the second round of pull tests at Battelle's PSF. The drop in amplitude is believed to be a result of using a non-optimal arbitrary waveform generator after the proper one was damaged in shipping. The replacement card was digital and was not capable of properly sampling the 130 kHz waveform sent to the 1200V amplifier.



Figure 6-11. Photograph of pull rig at BJ Services' facility in Calgary, AB, CA.

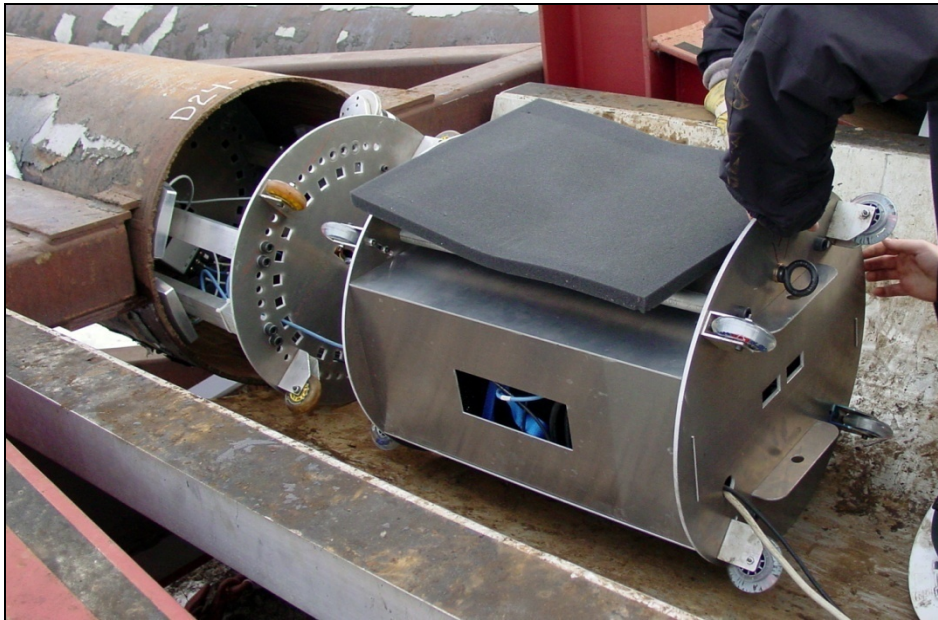


Figure 6-12. Photograph of prototype ILI tool showing sensor carriage (in pipe) and electronics carriage (on stage).

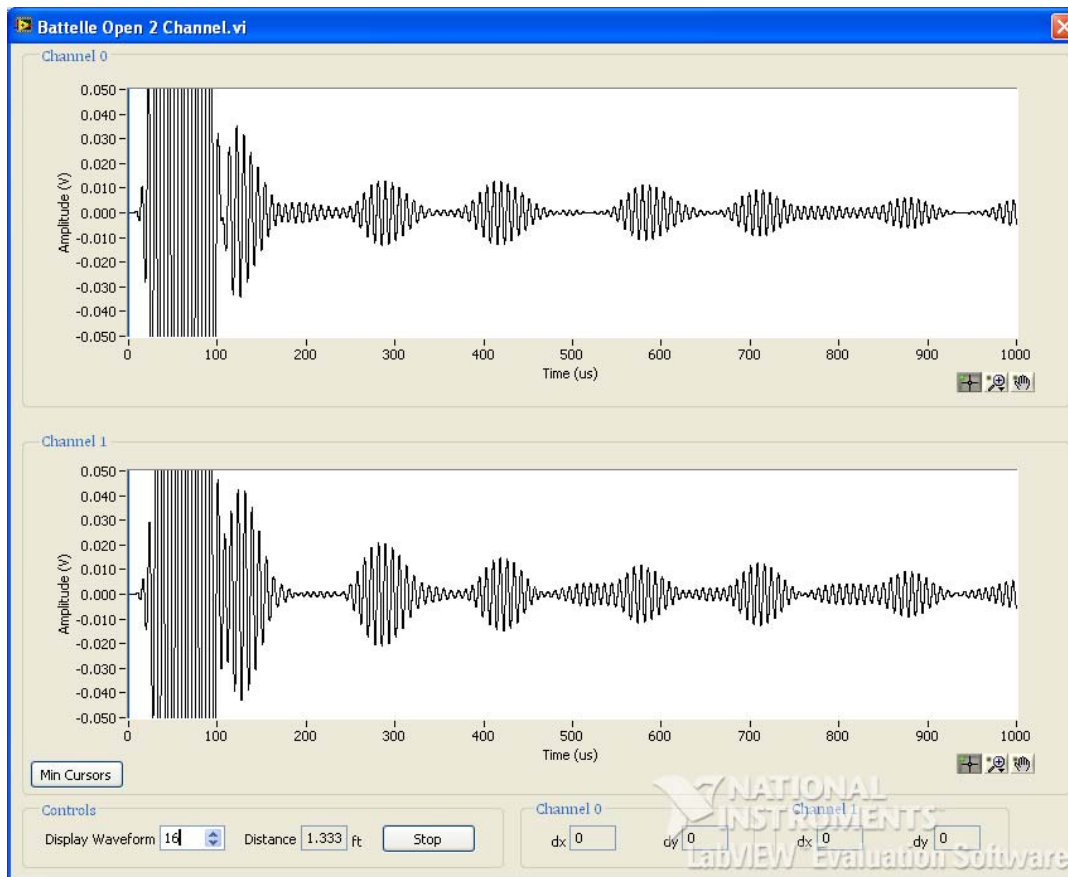


Figure 6-13. RF waveforms from two channels obtained during a hand-pull through a bare pipe specimen at BJ Services' facility.

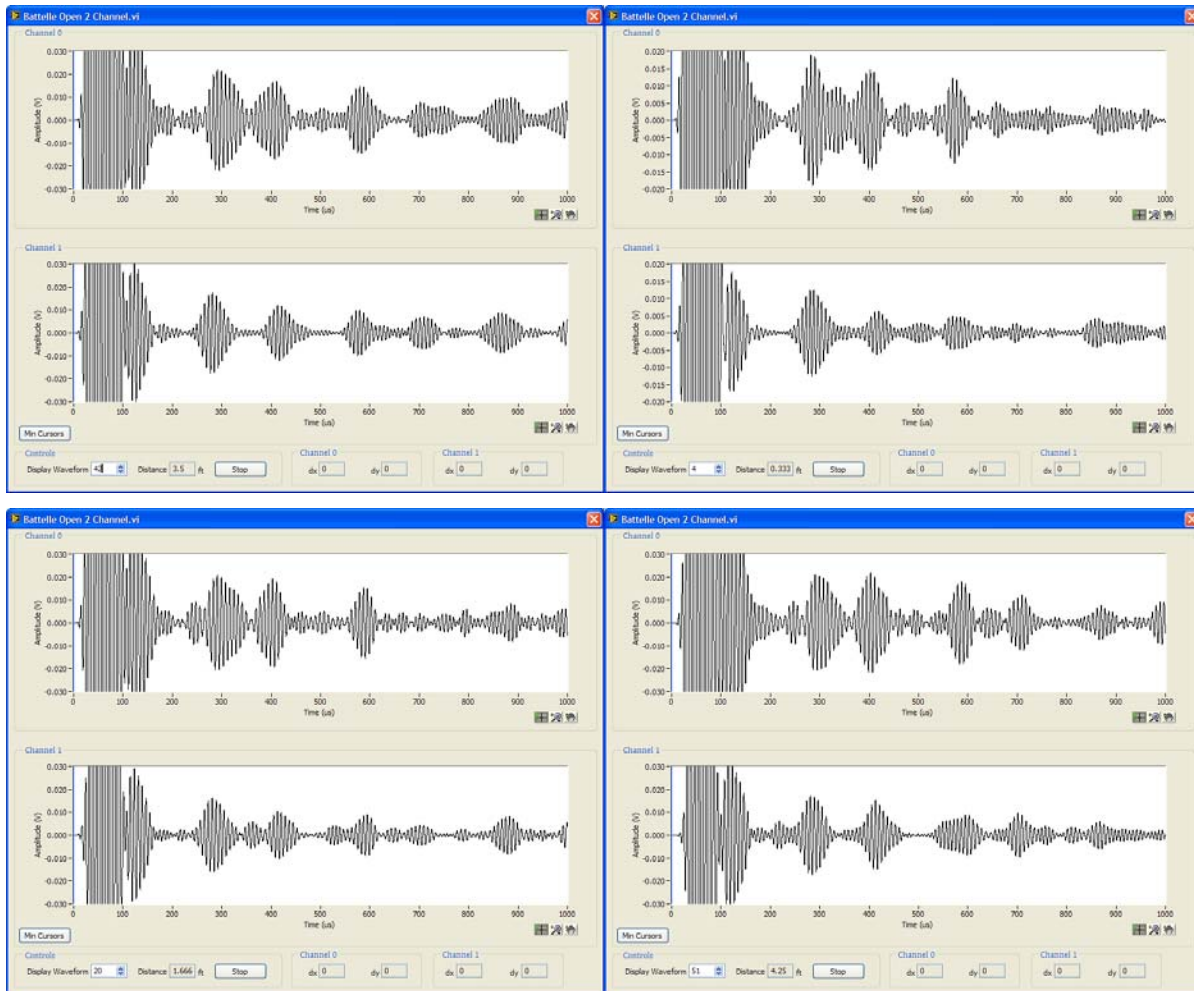


Figure 6-14. RF waveforms from several random locations obtained during pull tests through BJ Services’ pull rig.

Figure 6-14 shows the RF waveforms obtained from several random locations during the pull tests on BJ Services’ rig. The data from both channels are displayed on the same screen. In several of the waveforms there are elevated noise levels. It is believed that this was caused by a grounding issue within the sensor carrier. More work needs to be done to minimize electromagnetic noise.

After the data acquisition pulls were completed, the sensor carriage was pulled through the full length of the pull rig several times. Speeds ranged from 2 mph to 5 mph. Figure 6-15 shows a photograph of two of the sensor heads after the full-length pull tests were completed. Other than accumulating some debris, there was virtually no damage to the sensor heads. This demonstration showed that there is real potential for the development of sensor heads that are capable of withstanding the rigors of an actual ILI environment.

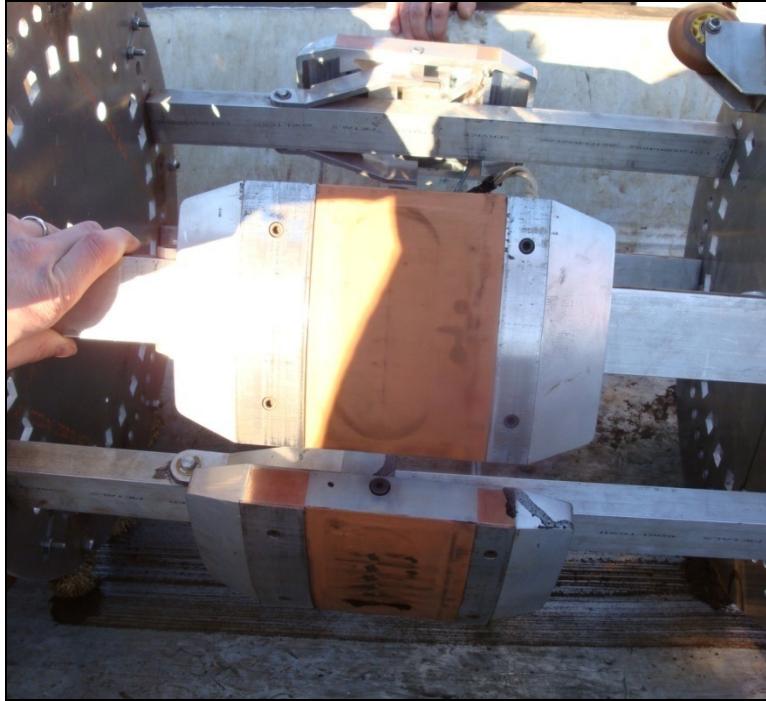


Figure 6-15. RF waveforms from two channels obtained during a hand-pull through a bare pipe specimen at BJ Services' facility.

6.4. Inspection Variables

Other inspection variables that were encountered throughout the several rounds of pull tests included the presence of girth and seam welds. Pipe 2, shown in Figure 6-3, contained two girth welds and it can be seen in the figure where the sensors rode over these girth welds at approximately 200 in. and 230 in.. It is possible to differentiate girth welds from other features by monitoring the amplitude of the reference packet. As the sensors ride over the weld, there is a dip in the amplitude of the reference packet.

Though the sensors never rode over a seam weld during any of the pull tests, it will inevitably happen in a real inspection environment. The anticipated result will be similar to riding over a girth weld, though it could potentially last for a much longer period of time. An amplitude dip in the reference packet will be observed but the amplitude-ratio between the reference packet and the complete traversal will remain constant.

Pipes containing much oxide debris could potentially affect the guided wave inspection negatively. This potential could be minimized by running a cleaning tool prior to running the guided wave tool.

7.0 Conclusion and Future Direction

The primary goal of this research effort was the development of a more reliable and robust guided-wave coating disbond detection technique than is currently available. Some of the key contributions of this work are outlined below:

- Development of N-layered dispersion codes for both SH- and Lamb-type waves traveling in the circumferential direction of a pipe. Analysis of the theoretical dispersion curves directly led to the identification of several features that are useful for disbond detection.
- Development of the N-layered wave structure analysis codes for both SH- and Lamb-type modes. Analysis of the wave structures directly aided in the selection of the wave modes and frequencies that have significant energy present at the pipe/coating interface.
- Comprehensive numerical modeling of circumferential guided waves in coated pipe. Models verified theoretical predictions and the validity of the proposed disbond detection features determined from theoretical analysis.
- Identification and experimental verification of time-, frequency-, and amplitude-based disbond detection features. Prior to this work, the time- and frequency-based features were never used for disbond detection.
- Development of a sensor arrangement such that all amplitudes can be normalized to some reference pulse, allowing for the more reliable use of amplitude-based features. This effectively accounts for such things as variation in sensor liftoff.
- Design and construction of a novel set of thick-trace transmitting and receiving PCB EMAT coils. These coils were designed very specially to be capable of handling the high current densities created by the 1200V amplifier.
- Experimental demonstration of coating disbond detection capability using an actual prototype EMAT ILI tool. All three disbond detection features were shown to perform well in an ILI environment.
- Experimental demonstration of coating disbond detection capability for thin (<1 mm) coatings using a time-based detection feature. Future work will be needed to optimize this technique through the selection of the ideal wave mode and frequency.

Though a significant contribution toward the reliable detection of coating disbonds using guided waves has been made, there is always more work to be completed. Perhaps the most logical next step of this work is the development of an optimized routine for disbond detection in thin coatings. This would involve further theoretical and numerical studies as well as the development of the supporting EMAT technologies capable of generating the desired modes and frequencies. Other future work may include the following:

- Development and demonstration of an automated disbond detection routine. At this point in time, all data analysis was performed manually. For an actual implementation, disbond detection would need to be done automatically as hundreds of thousands of data sets would need to be analyzed.

- Addition of SCC recognition capability. Though detection of axially oriented cracking was seen in one of the pull tests, a robust multi-feature recognition algorithm for SCC should be developed. As in the case of disbond detection, there are often less obvious features that are not currently in use that have great potential to aid in the detection and sizing of SCC.
- Development of robust corrosion sizing techniques specific to circumferential guided waves and ILI applications. Having multiple sensors pairs located around the circumference of the pipe allows for the development of some novel sizing methods.
- Further development of the EMAT sensor technology for use with ILI tools. There is still much work that can be done to ruggedize the sensor assemblies and improve the signal-to-noise ratio. The continued pursuit of an operational EDM EMAT coil could potentially have significant benefits in terms of both ruggedization and signal enhancement.

Because the guided-wave ILI market is still in its early developmental stages, and there are not many competing technologies available, there is significant opportunity to make lasting contributions in this area. It is strongly believed that some of the results of this work will eventually be incorporated into an industrial inspection technology. Aspects of this work have been presented at four different conferences, two of which were international conferences. The references to those works are as follows:

- Van Velsor, JK, Rose, JL (2008). "A Study of Circumferential Guided Wave Propagation in Multilayered Annular Structures." ASNT Fall Conference and Quality Testing Show 2008 Paper Summaries. Charleston, SC. The American Society for Nondestructive Testing.
- Van Velsor, JK, Rose, JL, Nestleroth, JB (2008). "Detection of Protective Coating Disbonds in Pipe Using Circumferential Guided Waves." 17th World Conference on Nondestructive Testing Paper Summaries, Shanghai, China.
- Van Velsor, JK, Rose, JL, Nestleroth, JB (2007). "Coating Disbond Detection in Pipe Using Circumferentially-Oriented Ultrasonic Guided Waves." ASNT Fall Conference and Quality Testing Show 2007 Paper Summaries. Las Vegas, NV. The American Society for Nondestructive Testing.
- Van Velsor, JK, Rose, JL, Nestleroth, JB, Owens, SE (2007). "Coating Disbond Detection in Pipe Using Circumferentially-Oriented Ultrasonic Guided Waves." 4th Middle East NDT Conference and Exhibition Paper Summaries, Kingdom of Bahrain, Saudi Arabian Section of the American Society for Nondestructive Testing.

Several refereed journal publications relating to this work are also under way.

8.0 References

1. Viktorov, I. A., *Rayleigh and Lamb Waves, Physical Theory and Applications*. Ultrasonic Technology, ed. L. Balamuth. 1967, New York: Plenum Press. 154.
2. Qu, J., Y. H. Berthelot, and Z. Li. *Dispersion of Guided Circumferential Waves in a Circular Annulus*. in *Review of Progress in Quantitative NDE*. 1996: American Institute of Physics, New York.
3. Liu, G. and J. Qu, "Guided Circumferential Waves in a Circular Annulus". *Journal of Applied Mechanics*, 1998. **65**: p. 424-430.
4. Rose, J. L., *Ultrasonic Waves in Solid Media*. 1st ed. 1999, Cambridge, UK: Cambridge University Press. 454.
5. Liu, G. and J. Qu, "Transient Wave Propagation in a Circular Annulus Subjected to Transient Excitation on its Outer Surface". *The Journal of the Acoustical Society of America*, 1998. **104**(3): p. 1210-1220.
6. Li, Z. and Y. H. Berthelot, "Propagation of Transient Ultrasound in Thick Annular Waveguides: Modeling, Experiments, and Application". *NDT&E International*, 2000. **33**: p. 225-232.
7. Valle, C., et al., "Crack Characterization Using Guided Circumferential Waves". *The Journal of the Acoustical Society of America*, 2001. **110**(3): p. 1282-1290.
8. Valle, C., J. Qu, and L. J. Jacobs, "Guided Circumferential Waves in Layered Cylinders". *International Journal of Engineering Sciences*, 1999. **37**: p. 1369-1387.
9. Towfighi, S., T. Kundu, and M. Ehsani, "Elastic Wave Propagation in Circumferential Direction in Anisotropic Cylindrical Curved Plates". *Journal of Applied Mechanics*, 2002. **69**: p. 283-291.
10. Jiandong, Y., W. Bin, and H. Cunfu, "Guided Circumferential Waves in Orthotropic Cylindrical Curved Plate and the Mode Conversion by the End-Reflection". *Applied Acoustics*, 2007. **68**: p. 594-602.
11. Zhao, X. and J. L. Rose, "Guided Circumferential Shear Horizontal Waves in an Isotropic Hollow Cylinder". *The Journal of the Acoustical Society of America*, 2004. **115**(5): p. 1912-1916.
12. Nestleroth, J. B. and G.A. Alers, *Enhanced Implementation of MFL Using EMAT Sensors to Detect External Coating Disbondment*, in *PRCI Contract PR-3-9715 Final Report*. 2002, Technical Toolboxes: Houston, TX. p. 71.
13. Aaron, J., et al., *Development of an EMAT In-Line Inspection System for Detection, Discrimination, and Grading of Stress Corrosion Cracking in Pipelines*, in *DOE Award No. DE-FC26-01NT41154 Annual Technical Progress Report*. 2003, Tuboscope Pipeline Services: Houston, TX. p. 49.
14. Al-Qahtani, H., T. Beuker, and J. Damaschke. *In-Line Inspection with High-Resolution EMAT Technology Crack Detection and Coating Disbondment*. in *Proceedings of 20th International Conference on Pipeline Pigging, Integrity Assessment and Repair*. 2008. Houston, TX.